Semi-Inclusive Charged-Pion Electroproduction off Protons and Deuterons: Cross Sections, Ratios and Access to the Quark-Parton Model at Low Energies

R. Asaturyan,[1] R. Ent,[2,3] H. Mkrtchyan,[1] T. Navasardyan,[1] V. Tadevosyan,[1] G.S. Adams,[4] A. Ahmidouch,[5] T. Angelescu,[6] J. Arrington,[7] A. Asaturyan,[1] O.K. Baker,[2,3] N. Benmouna,[8] C. Bertoncini,[9] H.P. Blok,[10] W.U. Boeglin,[11] P.E. Bosted,[2,12] H. Breuer,[13] M.E. Christy,[3] S.H. Connell,[14] Y. Cui,[15] M.M. Dalton,[16] S. Danagoulian,[5] D. Day,[17] J.A. Dunne,[18] D. Dutta,[19] N. El Khayari,[15] H.C. Fenker,[2] V.V. Frolov,[20] L. Gan,[21] D. Gaskell,[2] K. Hafidi,[7] W. Hinton,[3] R.J. Holt,[7] T. Horn,[2] G. M. Huber,[22] E. Hungerford,[15] X. Jiang,[23] M. Jones,[2] K. Joo,[24] N. Kalantarians,[15] J.J. Kelly,[13] C.E. Keppel,[2,3] V. Kubarovsky,[2] Y. Li,[15] Y. Liang,[25] D. Mack,[2] S. P. Malace,[3] P. Markowitz,[11] E. McGrath,[26] P. McKee,[17] D.G. Meekins,[2] A. Mkrtchyan,[1] B. Moziak,[4] G. Niculescu,[26] I. Niculescu,[26] A.K. Opper,[25] T. Ostapenko,[27] P.E. Reimer,[7] J. Reinhold,[11] J. Roche,[2] S.E. Rock,[12] E. Schulte,[7] E. Segbefia,[3] C. Smith,[17] G.R. Smith,[2] P. Stoler,[4] L. Tang,[2,3] M. Ungaro,[4] A. Uzzle,[3] S. Vidakovic,[22] A. Villano,[4] W.F. Vulcan,[2] M. Wang,[12] G. Warren,[2] F. R. Wesselmann,[17] B. Wojtsekhowski,[2] S.A. Wood,[2] C. Xu,[22] L. Yuan,[3] and X. Zheng[7]

[1] *Yerevan Physics Institute, Yerevan 0036, Armenia*
[2] *Thomas Jefferson National Accelerator Facility, Newport News, Virginia 23606, USA*
[3] *Hampton University, Hampton, Virginia 23668, USA*
[4] *Rensselaer Polytechnic Institute, Troy, New York 12180, USA*
[5] *North Carolina A & T State University, Greensboro, North Carolina 27411, USA*
[6] *Bucharest University, Bucharest, Romania*
[7] *Physics Division, Argonne National Laboratory, Argonne, Illinois 60439, USA*
[8] *The George Washington University, Washington, D.C. 20052, USA*
[9] *Vassar College, Poughkeepsie, New York 12604, USA*
[10] *VU-University, 1081 HV Amsterdam, The Netherlands*
[11] *Florida International University, University Park, Florida 33199, USA*
[12] *University of Massachusetts Amherst, Amherst, Massachusetts 01003, USA*
[13] *University of Maryland, College Park, Maryland 20742, USA*
[14] *University of Johannesburg, Johannesburg, South Africa*
[15] *University of Houston, Houston, TX 77204, USA*
[16] *University of the Witwatersrand, Johannesburg, South Africa*
[17] *University of Virginia, Charlottesville, Virginia 22901, USA*
[18] *Mississippi State University, Mississippi State, Mississippi 39762, USA*
[19] *Triangle Universities Nuclear Laboratory and Duke University, Durham, North Carolina 27708, USA*
[20] *California Institute of Technology, Pasadena, California 91125, USA*
[21] *University of North Carolina Wilmington, Wilmington, North Carolina 28403, USA*
[22] *University of Regina, Regina, Saskatchewan, S4S 0A2, Canada*
[23] *Rutgers, The State University of New Jersey, Piscataway, New Jersey, 08855, USA*
[24] *University of Connecticut, Storrs, Connecticut 06269, USA*
[25] *Ohio University, Athens, Ohio 45071, USA*
[26] *James Madison University, Harrisonburg, Virginia 22807, USA*
[27] *Gettysburg College, Gettysburg, Pennsylvania 18103, USA*

(Dated: December 16, 2011)

A large set of cross sections for semi-inclusive electroproduction of charged pions ($\pi^{\pm}$) from both proton and deuteron targets was measured. The data are in the deep-inelastic scattering region with invariant mass squared $W^2 > 4$ GeV^2 (up to ≈ 7 GeV^2) and range in four-momentum transfer squared $2 < Q^2 < 4$ (GeV/c)^2, and cover a range in the Bjorken scaling variable $0.2 < x < 0.6$. The fractional energy of the pions spans a range $0.3 < z < 1$, with small transverse momenta with respect to the virtual-photon direction, $P_t^2 < 0.2$ (GeV/c)^2. The invariant mass that goes undetected, M_x or W', is in the nucleon resonance region, $W' < 2$ GeV. The new data conclusively show the onset of quark-hadron duality in this process, and the relation of this phenomenon to the high-energy factorization ansatz of electron-quark scattering and subsequent quark $\rightarrow$ pion production mechanisms. The x, z and P_t^2 dependences of several ratios (the ratios of favored-unfavored fragmentation functions, charged pion ratios, deuteron-hydrogen and aluminum-deuteron ratios for π^+ and π^-) have been studied. The ratios are found to be in good agreement with expectations based upon a high-energy quark-parton model description. We find the azimuthal dependences to be small, as compared to exclusive pion electroproduction, and consistent with theoretical expectations based on tree-level factorization in terms of transverse-momentum-dependent parton distribution and fragmentation functions. In the context of a simple model, the initial transverse momenta of d quarks are found to be slightly smaller than for u quarks, while the transverse momentum width of the

favored fragmentation function is about the same as for the unfavored one, and both fragmentation widths are larger than the quark widths.

PACS numbers: 13.60.Le, 13.87.Fh

I. INTRODUCTION

There has been a growing realization that understanding of the resonance region in inelastic scattering, and the interplay between resonance behavior and a high-energy scaling phenomenon in particular, represents a critical gap that must be filled if one is to fathom fully the nature of the quark–hadron transition in Quantum ChromoDynamics (QCD). The decade or so preceding the development of QCD saw tremendous effort devoted to describing hadronic interactions in terms of S-matrix theory and self-consistency relations. One of the profound discoveries of that era was the remarkable relationship between low-energy hadronic cross sections and their high-energy behavior, in which the former on average appears to mimic certain features of the latter.

At low energies, one expects the hadronic scattering amplitude to be dominated by just a few resonance poles. As the energy increases, the density of resonances in each partial wave, as well as the number of partial waves itself, grows, making it harder to identify contributions from individual resonances, and more useful to describe the scattering amplitude in terms of a sum of t-channel Regge poles and cuts. Progress towards synthesizing the two descriptions came with the development of finite-energy sum rules, relating dispersion integrals over the amplitudes at low energies to high-energy parameters.

The observation [1] of such a nontrivial relationship between inclusive electron–nucleon scattering cross sections at low energy, in the region dominated by the nucleon resonances, and that in the deep-inelastic scattering (DIS) regime at high energy, similarly predated QCD. Initial interpretations of this duality naturally used the theoretical tools available at the time, finite-energy sum rules or consistency relations between hadronic amplitudes inspired by the developments in Regge theory that occurred in the 1960s [2, 3]. With the advent of QCD, De Rújula, Georgi, and Politzer offered a qualitative explanation of Bloom-Gilman duality [4] in terms of either small or on-average-canceling higher-twist contributions, but a quantitative understanding of the origin of the duality phenomenon in QCD remains elusive, although some insight has been obtained through phenomenological model calculations [5].

Even if it remains counterintuitive that there should be a strong relationship between the resonance region, in which the lepton scatters from a target hadron traditionally treated as a bound system of massive constituent quarks, and the deep-inelastic region, where the lepton essentially scatters from a single free quark, it is essential to provide precise data on the onset of this phenomenon. In regions where single-quark scattering is well established, a rich plethora of nucleon structure information can be gathered from such reactions through the quark-parton model [6–8].

In this article, we will concentrate on the largely unexplored low-energy domain of semi-inclusive electron scattering, $eN \to e\pi^{\pm}X$, in which a charged pion $\pi^{\pm}$ is detected in the final state in coincidence with the scattered electron. The process of semi-inclusive deep-inelastic scattering (SIDIS) has been shown to factorize [9], in the high energy limit, into lepton-quark scattering followed by quark hadronization. Our focus will be on the process where a quark fragments into a pion, such that the electroproduced pion carries away a large fraction, but not all, of the exchanged virtual photon's energy.

The quark-hadron duality phenomenon has been predicted [10–12], and subsequently verified [13] for high-energy meson electroproduction. The relation of the duality phenomenon with the onset of factorization in electron-quark scattering and subsequent quark hadronization was also postulated and shown to hold in *e.g.* the SU(6) quark model [6–8, 12, 14]. If so, one obtains access to the virtue of semi-inclusive meson production, that lies in the ability to identify, in a partonic basis, individual quark species in the nucleon by tagging specific mesons in the final state, thereby enabling both the flavor and spin of quarks and antiquarks to be systematically determined. Ideally, one could even directly measure the quark transverse momentum dependence of the quark distribution functions $q(x, k_t)$ by detecting all particles produced in the hadronization process of the struck quark. A large set of pion electroproduction data from both hydrogen and deuterium targets has been obtained in experiment E00-108 spanning the nucleon resonance region. Cross sections for semi-inclusive electroproduction of charged pions ($\pi^{\pm}$) from both proton and deuteron targets were measured for $0.2 < x < 0.6$, $2 < Q^2 < 4$ (GeV/c)^2, $0.3 < z < 1$, and $P_t^2 < 0.2$ (GeV/c)^2. The results from this experiment permit a first study of a possible low-energy access to the quark-parton model, either directly through cross section measurements or indirectly through their ratios, possibly lowering the energy threshold to access the quark-parton model if higher-twist contributions would fully cancel.

In Section 2, we will describe in detail the relation between kinematical cuts to separate current and target region fragmentation events as optimally as possible, quark-hadron duality, and a low-energy onset of a factorized (or precociously factorized) description in terms of electron-quark scattering and subsequent hadronization of the struck (current) quark. In Section 3, we will relate the findings of earlier low-energy experiments to a quark-parton model description, and extensions thereof beyond the infinite momentum frame including azimuthal-angle and transverse-momentum dependences. Sections 4, 5

and 6 will cover the experimental details, the data analysis procedures, and the systematic uncertainties, respectively. Finally, Sections 7 and 8 will describe the experimental results in terms of dependences of ratios and cross sections on various kinematic variables, including some nuclear dependences, followed by the conclusions.

II. TOWARDS A HIGH-ENERGY DESCRIPTION OF SEMI-INCLUSIVE PION ELECTROPRODUCTION

A. Semi-Inclusive Deep Inelastic Scattering

In semi-inclusive deep inelastic scattering (SIDIS), a hadron h (in our case a charged pion $\pi^{\pm}$) is detected in coincidence with a scattered electron, with a sufficient amount of energy and momentum transferred in the scattering process. Under the latter conditions, the reaction can be seen as knockout of a quark and subsequent (independent) hadronization.

Fig. 1 gives a schematic picture of this process, including the kinematics. An electron with four-momentum $(E, \vec{k})$ scatters from a nucleon with mass M (taken to be the proton mass M_p at rest), resulting in a scattered electron with four-momentum $(E', \vec{k'})$, thereby exchanging a virtual photon with four-momentum $q = (\nu, \vec{q})$ with a quark. A meson with four momentum $m = (E_h, \vec{P}_h)$ is produced, with the residual hadronic system characterized by an invariant mass W'. As usual, the four-momentum transfer squared is defined as $Q^2 = -q^2$ and the Bjorken variable as $x = Q^2/2M\nu$. The latter can be interpreted as the fraction of the light-cone momentum of the target nucleon carried by the struck quark. Furthermore, z is defined as $z = (p \cdot m)/(p \cdot q)$. In the target rest (lab) frame, this becomes $z = E_h/\nu$, the fraction of the virtual photon energy taken away by the meson. In the elastic limit, $z = 1$, and the meson carries away all of the photon's energy. Finally, we define P_t to be the transverse momentum of the meson in the virtual photon-nucleon system.

At high values of Q^2 and ν, the cross section (at leading order in the strong coupling constant α_s) for the reaction $N(e, e'\pi)X$ can be written in the following way (see Ref. [15]),

$$\frac{\frac{d\sigma}{d\Omega_e dE_e dz dP_t^2 d\phi}}{\frac{d\sigma}{d\Omega_e dE_e}} = \frac{dN}{dz} b e^{-bP_t^2} \frac{1 + A\cos(\phi) + B\cos(2\phi)}{2\pi}, \qquad (1)$$

$$\frac{dN}{dz} \sim \sum_i e_i^2 \; q_i(x, Q^2) \; D_{q_i \to \pi}(z, Q^2),$$

where i denotes the quark flavor and e_i is the quark charge, and the fragmentation function $D_{q_i \to \pi}(z, Q^2)$ gives the probability for a quark to evolve into a pion π with a fraction z of the quark (or virtual photon) energy, $z = E_\pi/\nu$. The first part of this formula expresses that the cross section factorizes into the product of the virtual photon–quark interaction and the subsequent quark hadronization. A consequence of factorization is that the fragmentation function is independent of x, and the parton distribution function $q_i(x, Q^2)$ independent of z. Both parton distribution and fragmentation functions, however, depend on Q^2 through logarithmic Q^2 evolution [16]. The second part describes the dependence on the transverse momentum P_t, assumed to be Gaussian, and the general dependence [17] of the cross section in the unpolarized case on the angle ϕ, the angle between the electron scattering plane and the pion production plane, with A and B, reflecting the interference terms σ_{LT} and σ_{TT}, respectively, being functions of x, Q^2, z, P_t. An important variable for the analysis is the missing mass M_x, which is the invariant mass of the undetected residual system. Here we refer to this quantity as W' (M_x) to highlight the fact that *it could play a role analogous to W for duality in the inclusive case* [11]. If we neglect the pion mass, W'^2 is given by

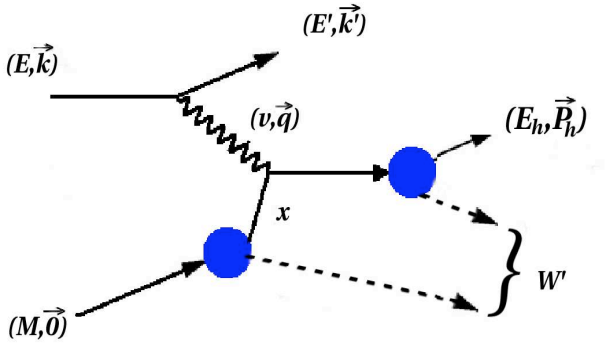

FIG. 1: Schematic diagram of meson electroproduction.

$$W'^2 = W^2 - 2z\nu\,(M + \nu - |\vec{q}|\,\cos\theta_{qm})\,, \qquad (2)$$

where $\nu = E - E'$ and θ_{qm} is the lab angle between the virtual photon momentum $|\vec{q}|$ and the outgoing meson momentum $|\vec{p}|$. As in the usual inclusive scattering case, the square of the (inclusive) invariant mass W is given by

$$W^2 = M^2 + Q^2\,(\frac{1}{x} - 1)\,. \qquad (3)$$

If we further limit the outgoing meson to be collinear with the virtual photon momentum and require that $Q^2/\nu^2 \ll 1$, we can express W'^2 in terms of z, x, and Q^2 as

$$W'^2 = M^2 + Q^2\,(1 - z)\,(\frac{1}{x} - 1)\,. \qquad (4)$$

The quantitative differences between Eqs. (2) and (4) are small for the described experimental results, and not visible on any of the figures in the remainder of this article.

For the remainder of this article, we will equate the "nucleon resonance region" to the condition that $W' < 2$ GeV, even if the invariant mass W will be beyond the

usually defined resonance region, $W > 2$ GeV. As can be easily read from Eq. (4), the larger z the fewer hadronic states will be involved in the semi-inclusive pion electroproduction process, with $z = 1$ the (deep) exclusive limit.

B. Factorization

If one neglects the dependence of the cross section on the pion transverse momentum P_t and the angle ϕ, the SIDIS cross section as given in Eq. (1) can be written as

$$\sigma \propto \sum_i q_i(x, Q^2)\ D_{q_i \to \pi}(z, Q^2). \tag{5}$$

(At higher orders one has to worry about gluon fragmentation functions, but this can be neglected for the energy and momentum transfers under consideration here [18]). The question is how well this factorization into independent functions of x and z is fulfilled in practice.

Initial investigations of the hadronization process were made in electron–positron annihilation and in deep inelastic scattering. By now a wealth of data has been accumulated to parameterize the fragmentation functions as function of z and Q^2. It is well known that for the case of SIDIS one has to worry about separating pions directly produced by the struck quark (termed "current fragmentation") from those originating from the spectator quark system ("target fragmentation"). This has been historically done for high-energy SIDIS by using separation in rapidity, η, with the latter defined in terms of the produced pion energy and the longitudinal component of the momentum (along the $\vec{q}$ direction),

$$\eta \ = \ \frac{1}{2} \ln \left(\frac{E_\pi - p_\pi^z}{E_\pi + p_\pi^z} \right) \ . \tag{6}$$

Early data from CERN [19, 20] suggest that a difference in rapidities, $\Delta\eta$, between pions produced in the current and target fragmentation regions ("rapidity gap") of at least $\Delta\eta \approx 2$ is needed to kinematically separate the two regions.

It has been argued that such kinematic separation is even possible at lower energies, or low W^2, if one considers only electroproduced pions with large elasticity z, *i.e.*, with energies close to the maximum energy transfer [20, 21]. Figure 2 shows a plot of rapidity versus z for $W = 2.5$ GeV. At $W = 2.5$ GeV, a rapidity gap of $\Delta\eta \geq 2$ would be obtained with $z > 0.4$ for pion electroproduction. For larger W, such a rapidity gap could already be attained at a lower value of z (see Ref. [21, 22]). For instance, one would anticipate a reasonable kinematic separation between the current and target fragmentation processes for $z > 0.2$ at $W = 5$ GeV. The other issue is at which energy scales we can make the assumption of independence of the hard scattering process from the hadronization process. At low energies we would normally view the nucleon as a collection of constituent quarks, and the factorization ansatz could break down due to effects of final state interactions, resonant nucleon excitations and higher-twist contributions [23], even if a sufficient rapidity gap would be established. For this article, we will simply assume that factorization in terms of a hard scattering and subsequent hadronization (called kinematical factorization in the remainder of this article) holds *provided* kinematical separation between current and target fragmentation is possible, *and* one is beyond the nucleon resonance region, $W' > 2$ GeV.

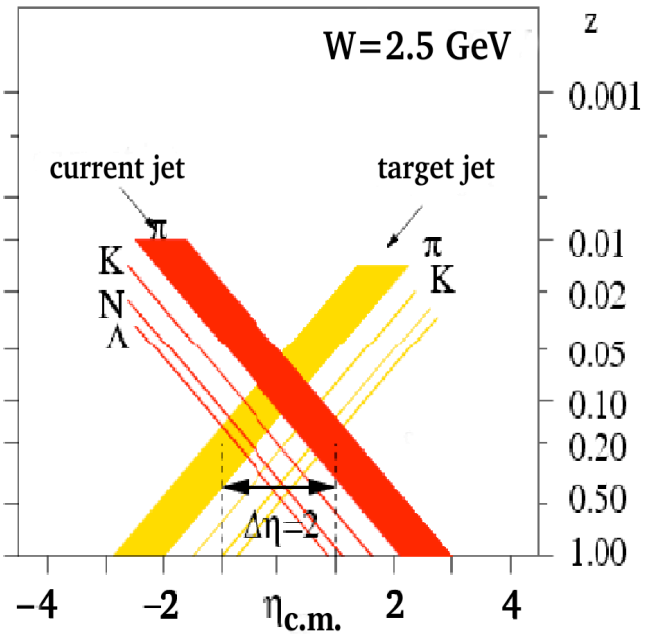

FIG. 2: (Color online) Relation between elasticity z and center of mass rapidity η_{CM} in semi-inclusive electroproduction of various hadrons for $W = 2.5\ GeV$, assuming null transverse momentum. The band for pions reflects the influence of transverse momentum.

To give credence to the latter assumption, we observe that in the annihilation process $e^+e^- \to hX$, experimental data [24, 25] beyond $z \approx 0.5$ at $W = 3$ GeV ($W' = 1.94$ GeV) were historically described in terms of fragmentation functions. The region extends to $z \geq 0.2$ for $W = 4.8$ GeV ($W' = 2.84$ GeV) and to $z \geq 0.1$ for $W = 7.4$ GeV ($W' = 4.14$ GeV). For $z > 0.3$, fragmentation functions have also been obtained from data [26] on $ep \to e'\pi^{\pm}X$ at an incident energy $E = 11.5$ GeV, with $3 < W < 4$ GeV. All of these data are beyond the ($W' > 2$ GeV) nucleon resonance region as defined above, and seem indeed reasonably well understood in terms of a simple fragmentation description.

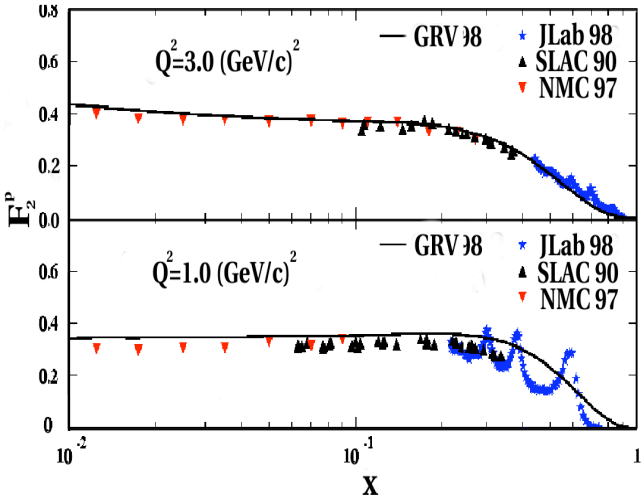

FIG. 3: (Color online) The structure function F_2 versus x for resonance data from Jefferson Lab and SLAC [29, 31], and SLAC and NMC deep-inelastic data, at two different values of Q^2. The solid curves show the GRV parameterization [32] at $Q^2 = 3$ (GeV/c)^2 and $Q^2 = 1$ (GeV/c)^2.

C. Quark-Hadron Duality and Precocious Factorization

At energies $W' < 2$ GeV, it is not obvious that the pion electroproduction process factorizes in the same manner as in Eq. (1). At energies where hadronic phenomena dominate, the pion electroproduction process may rather be described through the excitation of nucleon resonances, N^*, and their subsequent decays into mesons and lower lying resonances, N'^* [23, 27]. It has been argued that a factorization similar to the one at high-energy may appear to hold at low energies due to the quark-hadron duality phenomenon [10–12]. For that phenomenon to occur, non-trivial cancellations of the angular distributions from various decay channels [12, 27, 28] would be required to produce the fast-forward moving pion at the high-energy limit.

In the early 1970s, Bloom and Gilman made the phenomenological observation that there exists a duality between inelastic electron-proton scattering in the resonance region and in the Deep-Inelastic Scattering (DIS) regime [1]. More detailed studies over the last decade have shown that quark-hadron duality is exhibited over a broader kinematic range, and with greater precision, than was previously known [29, 30]. Duality was found to also work quite well locally, with various resonance regions averaging to DIS scaling expectations to good approximation ($< 10\%$), even down to low momentum transfer values ($Q^2 \approx 0.5$ (GeV/c)^2. Alternatively, the individual resonance scans average to *some global* curve even down to $Q^2 \approx 0.1$ (GeV/c)^2 [29, 31]. This global curve then coincides with the DIS scaling expectations at larger Q^2 (or x). This is illustrated in Fig. 3. The observation of duality tells us that higher twist terms mostly cancel, or are small, even at these low values of Q^2, when averaging over a sufficient (but relatively small) amount of resonances and the underlying non-resonant background contributions. This implies that single-quark scattering remains the dominant process, even though one visually can see the effect of the quark-quark interactions by the resonance peak enhancements. The quark-quark interactions modify the measured spectrum, bound to create confined quarks, but do so only locally.

Duality studies in inclusive scattering have been extended to spin-structure functions, which was predicted from both perturbative [33] and nonperturbative QCD arguments [12, 34]. The first experiment accessing the spin-dependent asymmetries was SLAC experiment E143 [35–37]. Spin asymmetry data reported by the HERMES Collaboration [38] and JLab (CLAS [39] and Hall A [40]) in the nucleon resonance region were also found to be in reasonable agreement with those measured in the deep-inelastic region [37, 41–43], with possible exceptions in the $N - \Delta$ resonance region. More recently, both CLAS and Hall A Collaborations have accumulated a set of precision data to study the onset of quark-hadron duality in polarized inclusive electron-nucleon scattering as function of Q^2 [40, 44], with good agreement found at larger Q^2 (> 2 (GeV/c)^2).

While the phenomenon of duality in inclusive electron scattering is thus well-established, duality in the related case of semi-inclusive meson electroproduction was not experimentally tested before this experiment. To experimentally investigate the existence of quark-hadron duality in semi-inclusive pion electroproduction processes, and how this may be related to a precocious (low-energy) factorization and partonic description, was one of the main goals of the E00-108 experiment.

Carlson [10] suggested several phenomena one could look for to explore any possible dual behavior between electroproduction of mesons in the resonance region and the high-energy scaling expectations by using 'meson tagging' in the final state, in close analogy to the original inclusive case findings by Bloom and Gilman [1]:

- Do we observe scaling behavior as Q^2 increases?
- Do the resonances tend to fall along the DIS scaling curve?
- Does the ratio of resonant to non-resonant strength remain roughly constant with increase of Q^2, as was one of Bloom-Gilman's original observations?

Existing experimental charged pion electroproduction data show hardly any nucleon resonance structure at $W' > 1.4$ GeV, and seem to scale [45], hinting at partial answers to some of these questions. In addition, an initial investigation of duality in semi-inclusive pion production was made in Ref. [12], where the factorization between parton distribution and fragmentation functions was found to hold when summing over the N* resonances in the SU(6) quark model.

The existence of low-energy kinematical factorization [12, 46] in combination with the quark-hadron duality phenomenon may very well lead to a precocious description of the SIDIS process at low energy in terms of the quark-parton model. Applying that to the case discussed here, one could anticipate that factorization and a quark-parton model description work reasonably well for $z > 0.4$ and at relatively low W' scales (below 2 GeV).

In this discussion we have neglected the dependence of measured pion yields, as in Eq. (5), on the pion transverse momentum, P_t. At high energies the dependence on P_t has historically been described with a Gaussian dependence as $\exp(-bP_t^2)$, where b^{-1} represents the average transverse momentum squared of the struck quark. At lower energies, the measured P_t dependence must reflect to some extent the decay angular distributions of the electroproduced resonances in regions where these resonances dominate. One would therefore expect the P_t dependence to vary with W' at low W'.

III. SEMI-INCLUSIVE DEEP INELASTIC SCATTERING AND THE QUARK-PARTON MODEL

In this Section we will first revisit experimental information at relatively low energies, in order to see if that exhibits characteristics of a factorized description as portrayed by Eq. (5). Theoretically, such a factorized description is only valid at leading order in α_s, and after integration over the transverse momentum P_t and the azimuthal angle ϕ. Then, we will investigate what can be learned from a phenomenological description of measurements of such transverse momenta and azimuthal angles, where the factorized description breaks down even at leading order, and a whole series of further assumptions must be made to relate these data to a quark-parton description.

A. Low-Energy $x - z$ Factorization and the Quark-Parton Model

Several pieces of evidence suggest that factorization may hold at low energies in meson-tagged reactions. Initially, skepticism existed about the applicability of the quark-parton model at energies below those historically used at, *e.g.*, the Electron Muon Collaboration experiment [47], because of the possibility of overlapping current and target fragmentation regions. Interest grew with the findings of the HERMES experiment at DESY, where an intriguing similarity was found between results from semi-inclusive deep inelastic scattering at moderate energies [48] and a Drell-Yan experiment at far higher energies [49]. This similarity suggested that factorization, and a quark-parton model description may after all be valid at energies where it is not necessarily expected to work.

The HERMES experiment measured semi-inclusive pion electroproduction ($\gamma^* N \rightarrow \pi^{\pm} X$) in the DIS regime, over the ranges $13 < \nu < 19$ GeV and $21 < W^2 < 35$ $(\mathrm{GeV})^2$, with an average four-momentum transfer $\langle Q^2 \rangle = 2.3$ $(\mathrm{GeV}/c)^2$. The HERMES analysis explicitly assumed factorization in order to extract the sea asymmetry $\overline{d} - \overline{u}$. In particular, it was assumed that the charged pion yield $N^{\pi^{\pm}}$ factorized into quark density distributions $q_i(x)$ and fragmentation functions $D_{q_i}^{\pi^{\pm}}(z)$:

$$N^{\pi^{\pm}}(x,z) \propto \sum_i e_i^2 \left[q_i(x)\, D_{q_i}^{\pi^{\pm}}(z) + \overline{q}_i(x)\, D_{\overline{q}_i}^{\pi^{\pm}}(z) \right] \tag{7}$$

Indeed, agreement was found between the extracted flavor asymmetry of the nucleon quarks sea results of HERMES, and the FermiLab Drell-Yan experiment E866 that first reported this flavor asymmetry (at dramatically higher energies). Revisiting these HERMES data, at an average $W > 5$ GeV, and constrained to fractions of the virtual photon energy, z, of larger than 0.2, it is perhaps not so surprising that these data support that the factorization assumption used in the HERMES analysis appears to be valid for the nucleon sea, even at relatively low energy loss. A rapidity gap $\eta > 2$, rendering potential sufficient separation between the current and target fragmentation regions and thus kinematical factorization, can already be attained at values of z of 0.2 (see Ref. [21, 22]) for $W = 5$ GeV. Given that in the HERMES kinematics also W' remains larger than 2 GeV, both requirements we assumed to be needed for a valid high-energy factorized description are fulfilled.

At even lower energies, with kinematics close to the experiment reported upon here, a series of measurements of semi-inclusive pion electroproduction was carried out at Cornell in the mid 1970s, with both hydrogen and deuterium targets [50–52]. These Cornell measurements covered a region in Q^2 ($1 < Q^2 < 4$ $(\mathrm{GeV}/c)^2$) and ν ($2.5 < \nu < 6$ GeV). The results of these measurements were analyzed in terms of an invariant structure function (comparable to $N^{\pi^{\pm}}(x,z)$ of Eq. 7), written in terms of the sum of products of parton distribution functions and parton fragmentation functions. The authors concluded that this invariant structure function shows no Q^2 dependence, and a weak dependence on W^2, within their region of kinematics, which would be consistent with a factorized quark-parton model description.

This is the more striking if one realizes that the Cornell kinematics cover a region in W^2 between 4 and 10 GeV^2, and in z between 0.1 and 1. In fact, if one would calculate W', these results are for an appreciable fraction of their kinematics in the region $1 < W' < 2$ GeV, which is generally associated with the nucleon resonance region. Even more, the final pion momentum is often only 1 GeV/c, such that final pion-nucleon scattering effects, especially differences between both pion charge flavors, cannot be neglected. To complete this enumeration, P_t, the average transverse momentum of the meson, was typically less than 0.1 GeV/c. Unfortunately, not enough statistics

and information are available to warrant a careful check of duality or factorization in the Cornell data, even if the data are suggestive that quark-hadron duality in charged pion electroproduction, and a precocious low-energy factorization, may work in these kinematics.

B. Transverse momenta and azimuthal angles

A central question in the understanding of nucleon structure is the orbital motion of partons. Much is known about the light-cone momentum fraction, x, and virtuality scale, Q^2, dependences of the up and down quark parton distribution functions (PDFs) in the nucleon. In contrast, very little is presently known about the dependence of these functions on the transverse momentum k_t of the parton. Simply based on the size of the nucleon in which the quarks are confined, one would expect characteristic transverse momenta of order a few hundred MeV/c, with larger values at small Bjorken x, where the sea quarks dominate, and smaller values at high x, where all of the quark momentum is longitudinal in the limit $x = 1$. Increasingly precise studies of the nucleon spin sum rule [53–56] strongly suggest that the net spin carried by quarks and gluons is relatively small, and therefore the net orbital angular momentum must be significant. This in turn implies significant transverse momentum of quarks. Questions that naturally arise include: what is the flavor and helicity dependence of the transverse motion of quarks and gluons, and can these be modeled theoretically and measured experimentally?

In the E00-108 experiment, we detect only a single hadronization product: a charged pion carrying a (large) energy fraction z of the available energy. The probability of producing a pion with a transverse momentum P_t relative to the virtual photon ($\vec{q}$) direction is described by a convolution of the quark distribution functions and p_t-dependent fragmentation functions $D^+(z, p_t)$ and $D^-(z, p_t)$, where p_t is the transverse momentum of the pion relative to the quark direction, k_t is the struck quark intrinsic transverse momentum, with the condition [57] $P_t = zk_t + p_t$. The "favored" and "unfavored" fragmentation functions $D^+(z, p_t)$ and $D^-(z, p_t)$ refer to the cases where the produced pion contains the flavor of the struck quark or not. "Soft" non-perturbative processes are expected [57] to generate relatively small values of p_t with an approximately Gaussian distribution in p_t. Hard QCD processes are expected to generate large non-Gaussian tails for $p_t > 1$ GeV/c, but probably do not play a major role in the interpretation of the E00-108 experiment, for which the total transverse momentum $P_t < 0.45$ GeV/c.

Because the average value of ϕ in the E00-108 experiment is correlated with P_t, (see Fig. 4), we first need to study the ϕ dependence. The cross sections for each target and pion flavor were parameterized in the form of Eq. 1. The assumed Gaussian P_t dependence (with slopes b for each case) is an effective parameterization that seems to describe the data adequately for use in making radiative and bin-centering corrections. Small values of A and B are expected from non-zero parton motion, as described by Cahn [58] and Levelt-Mulders [59]. In general, any non-zero parton motion effects, be it kinematic or dynamic, are proportional to P_t for A, and P_t^2 for B, respectively [58–61].

The more recent treatment of Ref. [57] similarly gives results for A and B that are very close to zero (especially for B). Other possible higher twist contributions will also be proportional to powers of $P_t/\sqrt{Q^2}$ [62, 63], and therefore suppressed at our low average values of P_t. Specifically, the twist-2 Boer-Mulders [64] contribution to B is essentially zero in the models of Ref. [64, 65]. For the kinematics of the E00-108 experiment, the value of B for π^+ is expected to be positive and could change approximately linearly with x, z and P_t from $\sim$0.002 to $\sim$0.02 GeV/c, see Fig. 6 and Fig. 7 in Ref. [66]. For π^-, it is expected to be negative and the dependences on x, z and P_t to be much weaker. In contrast, the values of A and B are much larger in exclusive pion production than those predicted for SIDIS.

IV. EXPERIMENT

The experiment E00-108 [67] ran in the summer of 2003 in Hall C at Jefferson Lab. An electron beam with energy of 5.479 GeV and currents ranging between 20 and 60 μA was provided by the CEBAF accelerator. Incident electrons were scattered from 4-cm-long liquid hydrogen or deuterium targets and detected in the Short Orbit Spectrometer (SOS). The SOS central momentum remained constant throughout the experiment, with a value of 1.702 GeV/c. The electroproduced mesons (predominantly pions) were detected in the High Momentum Spectrometer (HMS), with momenta ranging from 1.3 to 4.1 GeV/c. A detailed description of the spectrometers and set-up can be found in Ref. [68]. The experiment consisted of three parts: i) at a fixed electron kinematics of $(x, Q^2) = (0.32, 2.30\ (\mathrm{GeV}/c)^2)$, z was varied from 0.3 to 1 by changing the HMS momentum, with nearly uniform coverage in the pion azimuthal angle, ϕ, around the virtual photon direction, but at a small average P_t of 0.05 GeV/c (z-scan); ii) for $z = 0.55$, x was varied from 0.2 to 0.6, with a corresponding variation in Q^2 from 1.5 to 4.6 $(\mathrm{GeV}/c)^2$, by changing the SOS angle, keeping the pion centered on the virtual-photon direction (and again average P_t of 0.05 GeV/c) (x-scan); iii) for $(x, Q^2) = (0.32, 2.30\ (\mathrm{GeV}/c)^2)$, z near 0.55, P_t was scanned from 0 to 0.4 GeV/c by increasing the HMS angle (with average ϕ near 180 degrees) (P_t-scan). The kinematic settings are listed in Table I.

TABLE I: Kinematic settings (z-scan, x-scan and P_t-scan) in experiment E00-108. The electron beam energy E was 5.479 GeV. The scattered electrons were detected in SOS set at constant momentum 1.702 GeV/c throughout the experiment.

θ_e deg	ν GeV	Q^2 (GeV/c)^2	x	W^2 GeV^2	$\|\vec{q}\|$ GeV/c	θ_q deg	θ_m deg	z	p_m GeV/c	W'^2 GeV^2
28.71	3.794	2.30	0.32	5.70	4.09	11.54	11.54	0.37	1.397	3.92
								0.42	1.606	3.65
								0.49	1.846	3.35
								0.56	2.122	3.00
								0.64	2.439	2.60
								0.74	2.803	2.13
								0.85	3.222	1.60
								0.97	3.703	1.00
25.70	3.794	1.85	0.26	6.16	4.03	10.55	10.55	0.55	2.082	3.25
28.71	3.794	2.30	0.32	5.70	4.09	11.54	11.54	0.55	2.082	3.05
31.75	3.794	2.80	0.39	5.20	4.15	12.47	12.47	0.55	2.082	2.82
34.55	3.794	3.30	0.46	4.70	4.21	13.27	13.27	0.55	2.082	2.60
37.17	3.794	3.80	0.53	4.20	4.27	13.95	13.95	0.55	2.082	2.37
39.63	3.794	4.30	0.60	3.70	4.32	14.54	14.54	0.55	2.082	2.15
28.71	3.794	2.30	0.32	5.70	4.09	11.54	11.54	0.55	2.082	3.29
						11.54	13.54	0.55	2.082	3.29
						11.54	15.54	0.55	2.082	3.29
						11.54	17.54	0.55	2.082	3.29
						11.54	19.54	0.55	2.082	3.29

The ϕ distribution as a function of P_t is shown for all three data sets combined in Fig. 4. Except for the largest x-setting in the x-scan, the virtual-photon-nucleon invariant mass W was always larger than 2.1 GeV (typically 2.4 GeV), in the traditional deep-inelastic region for inclusive scattering. In order to avoid complications from πN final-state interactions the momenta of the outgoing pions were kept greater than 2 GeV/c in most cases. All measurements were performed for both π^+ and π^-.

V. DATA ANALYSIS

The raw data collected by the data acquisition system were processed by the standard Hall C analysis engine (ENGINE), which decodes the data into physical quantities on an event by event basis. The main components of the data analysis include tracking, event reconstruction, determination of and correction for experimental and kinematic offsets, particle identification and event selection, background estimation and subtraction, correction for detector efficiencies, and electronic and computer dead times. Many steps of the analysis here are similar to the F_π data analysis described in Ref. [68]. Below we will discuss some of the steps, and will emphasize details relevant to the E00-108 experiment.

Accidentals: Random coincidences occur between events from any two beam bursts within the coincidence timing gate. The resulting coincidence timing structure of random coincidences is peaked every 2 ns (defined by the beam microstructure of the CEBAF accelerator). The random events under the real coincidence peak cannot be identified but their contribution can be estimated. The data were corrected for these random contributions by selecting a number of random peaks and subtracting their average content from the content of the real coincidence peak. The accidentals were taken for an ∼80 ns interval (for 40 bursts far from the coincidence peak ($e'\pi^-$ at negative polarity of the HMS spectrometer, and e'p and $e'\pi^+$ peaks at positive polarity)), and the average number of accidentals (within 2 ns) was defined as $N_{Accidentals}(\ 2\ \text{ns}) = [N_{Accidentals}\ (80\ \text{ns})]/40$.

Electron Identification: Electrons were identified in the SOS using a combination of the SOS gas Čerenkov detector and calorimeter. The gas Čerenkov detector was used as a threshold detector with a mean signal of ∼7 photoelectrons per electron. Good electron events were selected for a photoelectron (pe) cut $N_{pe} > 0.5$. This cut was chosen to ensure good efficiency over the full acceptance, even after accounting for the position dependence of the pe yield. To determine the efficiency of the Čerenkov detector, an electron sample was selected from data with the calorimeter cut $E_{cal}/P_{e^-} > 0.8$, where E_{cal} is a total energy deposited in the calorimeter, and P_{e^-} is the momentum of the particle in the electron arm (SOS) defined by tracking. The Čerenkov detector efficiency is then given by the ratio of events with and without the Čerenkov detector cut. The efficiency was found to be

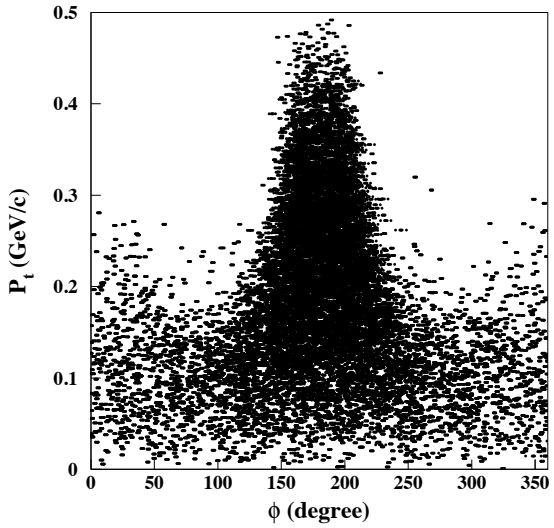

FIG. 4: P_t distribution of the data from this experiment as a function of azimuthal angle ϕ.

$\gtrsim 99.8\%$ for a photoelectron cut of $N_{pe} > 0.5$.

Electrons deposit their entire energy in the calorimeter peaking E_{cal}/P_{e^-} distribution at 1. Good electron events in the calorimeter were selected by applying the cut $E_{cal}/P_{e^-} > 0.7$. This cut removes most of the pions, while keeping high electron detection efficiency. The efficiency of the calorimeter was determined in a similar fashion as for the gas Čerenkov detector. A particle identification cut was placed on the gas Čerenkov detector, and the calorimeter efficiency was estimated as the ratio of events passing the calorimeter cut to the total number of events. The corresponding efficiency was estimated to be $\gtrsim 99.5 \pm 0.1\%$. The pion rejection factor (the ratio of pions with and without cut on energy deposition in calorimeter) in this case was $\sim$ 1:20.

Pion Identification: Pions in the HMS are selected with aerogel and gas Čerenkov detectors. The gas Čerenkov detector's function was to separate electrons from negatively-charged pions. The HMS calorimeter did not play a significant role and was used only for cross checks, and for the gas Čerenkov detector efficiency determination.

Pions under the Čerenkov radiation threshold do not in principle produce a signal in the detector. However, pions may produce δ-electrons, which will result in a photoelectron number greater than zero. Applying a cut to reject electrons may then reject pion events as well. To determine the pion efficiency of the Čerenkov detector cut positive polarity π^+ data were used with a calorimeter cut (to take out contribution from positrons). The ratio of events passing the Čerenkov detector cut to all the events is then the Čerenkov detector pion efficiency. The pion Čerenkov detector efficiency is $99.6 \pm 0.05\%$ for a cut $N_{pe} < 2$.

The separation of pions from protons (and partly from kaons) relies on the HMS aerogel detector [69]. Whether or not a particle traversing the aerogel Čerenkov detector produces a signal depends on the index of refraction of the aerogel material (n_{ref}) and the particle velocity ($\beta = v/c$). The mean number of photoelectrons (for aerogel material with n_{ref}=1.015) was N_{pe} ∼7-8 and slightly varied with a particle momentum (for z-scan data). The aerogel Čerenkov detector efficiency is $99.5 \pm 0.02\%$ for a threshold cut of $N_{pe} > 1$.

Real electron-proton coincidences are eliminated via coincidence time cuts in the analysis. In all kinematic settings of the experiment the electron-hadron coincidence time distribution is well described by Gaussian with $\sigma \leq 250$ ps (in average). In the analysis a cut ± 1.2 ns is used on the e-π coincidence time. At the highest momentum setting of the HMS (P_{HMS}=4.1 GeV/c), which is the worst case, there is still about 3 ns separation between electron-proton and electron-pion coincidence peaks. Even in the absence of proton rejection from the aerogel Čerenkov detector, the protons (and partly kaons at low momenta) would be removed in the random subtraction.

A. Background subtraction and corrections

Contribution from Target Walls: Events from the aluminum walls of the cryogenic target cell were subtracted by performing empty target runs (*dummy runs*). The *dummy data* are analyzed in the same way as the regular data including the same method of random coincidence subtraction and applying the same analysis cuts. The effective charge-normalized yields are then subtracted from the real data yields taking into account the difference in the wall thickness between the target cell (0.133 mm) and dummy target (1 mm). In most cases, the estimated contribution of the target can to the measured yield is quite small, about $2-3\%$. The uncertainty in the ratio of the thickness of the dummy relative to the target can ($2-3\%$) contributes to a negligible uncertainty to the total yield.

Radiative Corrections: Essentially all of the events that "radiate in" to a given bin come from either: (i) incoming electrons with a lower actual energy than the nominal beam energy, because they have radiated a photon; or (ii) scattered electrons with higher energy than the one measured in the spectrometer, because they radiated a photon. In both cases, the value of ν at the vertex is lower than the reconstructed one, hence z is larger and W' is smaller than the nominal value.

The radiative tails within our semi-inclusive pion electroproduction data were estimated using the Monte Carlo package SIMC. The radiative correction formula coded is based on the work of Mo and Tsai [70], which originally was derived for inclusive electron scattering, but was modified for use in coincidence experiments [71]. Details

TABLE II: The values of radiative corrections for x-scan data.

x	z	Q^2 (GeV/c)^2	π^+_H (%)	π^-_H (%)	π^+_D (%)	π^-_D (%)
0.22	0.55	1.59	4.2±0.4	5.6±0.6	4.6±0.5	5.4±0.5
0.26	0.55	1.88	4.5±0.5	5.8±0.6	4.9±0.5	5.6±0.6
0.30	0.55	2.17	4.9±0.5	6.2±0.6	5.2±0.5	5.9±0.6
0.34	0.55	2.46	5.3±0.5	6.5±0.7	5.6±0.6	6.3±0.6
0.38	0.55	2.75	5.8±0.6	6.9±0.7	6.1±0.6	6.7±0.7
0.42	0.55	3.04	6.2±0.6	7.4±0.7	6.5±0.7	7.1±0.7
0.46	0.55	3.32	6.8±0.7	7.8±0.8	7.0±0.7	7.5±0.8
0.50	0.55	3.61	7.3±0.7	8.3±0.8	7.5±0.8	8.0±0.8
0.54	0.55	3.90	7.9±0.8	8.9±0.9	8.1±0.8	8.5±0.9
0.58	0.55	4.19	8.5±0.9	9.4±0.9	8.7±0.9	9.1±0.9

TABLE III: The values of radiative corrections for z-scan data.

x	z	Q^2 (GeV/c)^2	π^+_H (%)	π^-_H (%)	π^+_D (%)	π^-_D (%)
0.32	0.37	2.31	1.6±0.2	3.3±0.3	2.1±0.2	3.2±0.3
0.32	0.42	2.31	2.4±0.2	4.1±0.4	2.8±0.3	3.9±0.4
0.32	0.49	2.31	3.4±0.3	5.1±0.5	3.8±0.4	4.8±0.5
0.32	0.55	2.31	4.5±0.5	6.2±0.6	4.9±0.5	5.8±0.6
0.32	0.64	2.31	5.9±0.6	7.5±0.8	6.2±0.6	7.0±0.7
0.32	0.74	2.31	7.8±0.8	9.3±0.9	8.1±0.8	8.8±0.9
0.32	0.85	2.31	10.8±1.1	11.9±1.2	11.0±1.1	11.5±1.2
0.32	0.97	2.31	18.3±1.3	18.5±1.9	18.3±1.8	18.3±1.8

of the implementation are described in Ref. [72]. The original formulation of the radiative correction procedure used in SIMC was for $(e, e'p)$ reaction. The formula were extended to pion electroproduction by D. Gaskell [73].

As a cross-check, we also estimated radiative corrections using the code POLRAD. The standard FORTRAN code POLRAD-2.0 [74] was written for radiative correction (RC) calculations in inclusive and semi-inclusive deep-inelastic scattering of polarized leptons by polarized nucleons and nuclei. The program, which is based theoretically on the original approach proposed in the Ref. [75], was created to suit the demands of experiments with fixed polarized nuclear targets and at a collider. A new version of POLRAD [76] was created to calculate the RC for semi-inclusive (polarized) experiments. In this case the cross section depends additionally on the variable z.

The radiative corrections calculated with POLRAD-2.0 are in good agreement with SIMC. On average the RC's are on the level of $\sim 6-8\%$ for all our data sets at $z < 0.7$ and reach $\sim 15\%$ at $z \gtrsim 0.9$. The relative values of radiative corrections at our kinematic settings are listed in Tables II, III and IV.

Exclusive Pions: In addition, we subtracted radiative events coming from the exclusive reactions $e + p \to e' + \pi^+ + n$ and $e + n \to e' + \pi^- + p$. This required a model for the cross section of exclusive pion electroproduction that is valid for a large range of W (from the resonance region to $W \approx 2.5$ GeV) at relatively large Q^2. The model used in this analysis started with the parameterization of exclusive π^+ and π^- production cross section data from [77] at $W \approx 2.2$ GeV and $Q^2 = 0.7$ and 1.35 (GeV/c)^2. This parameterization describes the more recent data taken at Jefferson Lab as part of the Charged Pion Form Factor program [68, 78, 79] ($W = 1.95$ GeV, Q^2=0.6−1.6 (GeV/c)^2 and $W = 2.2$ GeV, Q^2=1.6, 2.45 (GeV/c)^2) reasonably well.

TABLE IV: The values of radiative corrections for P_t-scan data. Note, for this set of measurements the scattered electron kinematic was fixed at Q^2=2.31 $(GeV/c)^2$

x	z	P_t^2 (GeV/c)^2	π^+_H (%)	π^-_H (%)	π^+_D (%)	π^-_D (%)
0.32	0.55	0.01	6.3±0.5	7.9±0.7	6.4±0.5	7.4±0.5
0.32	0.55	0.03	5.4±0.7	6.7±0.7	5.4±0.7	6.1±0.7
0.32	0.55	0.05	4.7±0.7	5.9±0.7	4.3±0.7	5.0±0.7
0.32	0.55	0.07	3.9±0.6	4.9±0.6	4.8±0.6	5.5±0.6
0.32	0.55	0.09	1.4±0.7	2.2±0.7	3.3±0.7	3.9±0.7
0.32	0.55	0.11	1.4±0.7	2.2±0.8	2.5±0.7	3.1±0.8
0.32	0.55	0.13	-1.6±0.9	-1.0±0.9	-0.8±0.9	-0.1±0.9
0.32	0.55	0.15	-1.4±1.2	-0.7±1.2	-1.5±1.2	-0.8±1.2
0.32	0.55	0.17	-3.9±1.8	-3.4±1.9	-1.1±1.8	-0.5±1.8
0.32	0.55	0.19	-8.3±3.2	-7.9±3.3	-5.7±3.2	-5.3±3.2

While the starting parameterization is appropriate for describing exclusive pion production above the resonance region, it does rather poorly for values of W significantly smaller than 2 GeV. Since no existing model or parameterization describes exclusive pion production both in the resonance region and at large W, we chose to adjust our starting model by-hand to give good agreement with the MAID model [80] of pion electroproduction in the resonance region. This by-hand adjustment began with the assumption that the longitudinal contribution was well described by the starting model, even at relatively low W. Discrepancies between the starting fit and the MAID calculation were attributed to the transverse cross section and were removed by assuming a more modest W dependence therein. We further simplified the model by assuming that the TT and LT interference terms mostly averaged to zero over our experimental acceptance so that they contributed negligibly to the radiative events.

We ran SIMC with this modified model for exclusive π^+ electroproduction on the proton and for π^+ and π^- production on the deuteron for all our kinematic settings (z-scan, x-scan and P_t-scan).

Contributions from exclusive pions were subtracted on a bin by bin basis. On average, the contribution from the exclusive tail was estimated to be 4-5% for the x-scan data, 5-15% for the z-scan data at $z < 0.8$, and 8-10% for the P_t-scan results (see Tables V, VI, and VII).

The radiative tail from exclusive events is the dominant correction for our data at $z > 0.8$. For $z \gtrsim 0.9$ the contributions from exclusive pions become more than 50%.

We also performed an alternative analysis using the code HAPRAD [81]. The two results agree to within $\pm 10-15\%$ in the relative contribution of the radiative

TABLE V: The relative contribution of radiative exclusive tail for x-scan data.

x	z	Q^2 (GeV/c)^2	π^+_H (%)	π^-_H (%)	π^+_D (%)	π^-_D (%)
0.22	0.55	1.59	6.1±0.2	-	3.7±0.1	5.1±0.2
0.26	0.55	1.88	5.2±0.1	-	3.5±0.1	5.1±0.1
0.30	0.55	2.17	4.6±0.1	-	3.4±0.1	5.3±0.1
0.34	0.55	2.46	4.6±0.1	-	3.3±0.1	5.1±0.1
0.38	0.55	2.75	4.2±0.1	-	2.9±0.1	4.8±0.1
0.42	0.55	3.04	3.8±0.1	-	2.7±0.1	4.9±0.1
0.46	0.55	3.32	3.7±0.1	-	2.6±0.1	4.2±0.1
0.50	0.55	3.61	3.1±0.1	-	2.3±0.1	3.6±0.1
0.54	0.55	3.90	3.2±0.1	-	1.9±0.1	3.1±0.1
0.58	0.55	4.19	2.5±0.1	-	1.5±0.1	2.5±0.1

TABLE VI: The relative contribution of radiative exclusive tail for z-scan data.

x	z	Q^2 (GeV/c)^2	π^+_H (%)	π^-_H (%)	π^+_D (%)	π^-_D (%)
0.32	0.33	2.31	3.6±0.2	-	2.6±0.1	3.6±0.2
0.32	0.38	2.31	3.9±0.1	-	3.1±0.1	4.6±0.1
0.32	0.44	2.31	4.3±0.1	-	3.4±0.1	4.7±0.1
0.32	0.50	2.31	4.1±0.1	-	2.8±0.1	5.0±0.1
0.32	0.55	2.31	5.9±0.1	-	4.4±0.1	7.6±0.1
0.32	0.61	2.31	7.5±0.1	-	5.8±0.1	8.7±0.2
0.32	0.66	2.31	8.8±0.1	-	6.4±0.1	10.3±0.2
0.32	0.72	2.31	11.0±0.2	-	7.7±0.1	12.2±0.2
0.32	0.78	2.31	13.8±0.2	-	8.7±0.2	15.1±0.3
0.32	0.83	2.31	15.7±0.3	-	9.5±0.2	18.0±0.4
0.32	0.89	2.31	21.8±0.4	-	15.0±0.3	30.3±0.6
0.32	0.94	2.31	$\gtrsim$90	-	$\gtrsim$90	$\gtrsim$90

exclusive tail. Thus, the resulting uncertainty is only at the 1% level or less.

Diffractive ρ: Some of the detected events may originate from the decay of diffractive vector meson production. The underlying physics of this process, which can be described as that the virtual photon fluctuates into a vector meson, which subsequently can interact with the nucleon through multiple gluon (Pomeron) exchange, is distinctively different from the interaction of a virtual photon with a single current quark. Again, we used SIMC to evaluate such a diffractive ρ meson contribution.

TABLE VII: The relative contribution of radiative exclusive tail for P_t-scan data. Note, for these measurements the value of four-momentum transfer square was kept at Q^2=2.31 (GeV/c)^2.

x	z	P_t^2 (GeV/c)^2	π^+_H (%)	π^-_H (%)	π^+_D (%)	π^-_D (%)
0.32	0.55	0.01	5.8±0.1	-	4.0±0.1	3.1±0.1
0.32	0.55	0.03	6.9±0.1	-	4.6±0.1	3.7±0.1
0.32	0.55	0.05	7.4±0.1	-	5.3±0.1	7.3±0.2
0.32	0.55	0.07	8.7±0.2	-	5.5±0.1	9.2±0.3
0.32	0.55	0.09	9.0±0.2	-	6.0±0.2	8.4±0.3
0.32	0.55	0.11	9.6±0.3	-	6.4±0.3	9.6±0.5
0.32	0.55	0.13	11.1±0.5	-	6.8±0.4	10.3±0.6
0.32	0.55	0.15	10.8±0.6	-	9.8±0.8	11.7±0.9
0.32	0.55	0.17	16.8±1.6	-	11.0±1.8	15.6±2.2
0.32	0.55	0.19	15.9±3.3	-	22.0±5.5	22.1±5.5

The p(e,e$'\rho^\circ$)p cross section calculation was based on the PYTHIA [82] generator, adopting similar modifications as implemented by the HERMES collaboration to describe lower-energy processes [83]. Additional modifications were implemented to improve agreement with ρ^0 cross section data from CLAS in Hall B at Jefferson Lab [84].

The p(e,e$'\rho^\circ$)p cross section can be written as

$$\sigma^{ep\to\rho p}(\nu,Q^2) = \Gamma_T\,(1+\epsilon R)\left(\frac{M_\rho^2}{M_\rho^2+Q^2}\right)^n \sigma^{\gamma p\to\rho p}, \tag{8}$$

where Γ_T is the transverse photon flux factor, $R=\sigma_L/\sigma_T$ is the ratio of longitudinal to transverse cross sections, $\left(\frac{M_\rho^2}{M_\rho^2+Q^2}\right)^n$ ($n=2$ in PYTHIA) is an additional factor that accounts for the suppression of the cross section from virtual photons, and $\sigma^{\gamma p\to\rho p}$ is the photoproduction cross section. The modifications to the PYTHIA model implemented for this analysis mimic those implemented by the HERMES collaboration:

1. The calculation of Γ_T was performed with no high-energy approximations
2. An improved parametrization of $R=\sigma_L/\sigma_T$
3. Replacement of the exponent $n=2$ with $n\approx 2.6$, more consistent with lower energy data

The t dependence of the ρ° cross section is parametrized as

$$\frac{d\sigma}{d|t'|} = \sigma^{ep\to\rho p}(\nu,Q^2) b e^{-b|t'|}, \tag{9}$$

where $t'=t-t_{min}$ (<0 for electroproduction) and b is the slope parameter. Note that at $t'=0$, b also impacts the overall scale of the forward cross section. The HERMES/PYTHIA model assumed a value of $b\approx 7$ GeV^{-2} for all energies. However, CLAS data suggested that this constant value of b did not adequately describe the t' dependence at JLab energies. The model used in SIMC fits b as a function of $c\Delta\tau$ (the vector meson formation time). Above $c\Delta\tau=2$ fm, b was taken to be a constant value of 7.0 GeV^{-2}, while for $c\Delta\tau<2$ fm, b increased from 1.0 GeV^{-2} to 7.0 GeV^{-2} between $c\Delta\tau=0.4$ fm and 2 fm.

Using the above model, the fraction of events due to pions from the decay of produced ρ mesons was estimated to range from a few percent at low z to about 15% at $z=0.6$, and was subtracted on bin by bin basis. The SIMC determination of the exclusive ρ° contribution to the semi-inclusive yield was also checked independently using a program and model developed by the CLAS collabration [85]. The two calculations were found to agree to about the 10% level.

Pion decay: Pion decay in flight is included in the Monte Carlo simulation. Charged pions predominantly decay via $\pi^{\pm} \rightarrow \mu^{\pm}\nu_{\mu}$ with a branching fraction of 99.99%. In SIMC the pion can decay at any point along its path in the magnet-free regions and at fixed points in the magnetic fields of the HMS. The muon momentum is calculated in the pion center-of-mass frame, where the angular distribution is uniform and the muon momentum is fixed. The muon is then followed through the spectrometer to the detector hut. Like in the experimental data, the muon is treated as if it were a pion in the reconstruction of target variables. In both the experimental and simulated data the muons constitute a background that is not removed by means of particle identification. However, the distribution of the muons in various reconstructed quantities is much broader than that of the pions. The fraction of pions decaying in flight on their way from the target can be calculated from the spectrometer central momentum and path length. While at low momentum roughly 20% of all pions decay on their way to the HMS detector hut, only a quarter of the muons fall within the acceptance and pass all cuts. More than 85% of all simulated muons that survive all cuts originate in the field free region behind the HMS dipole. We found the muon contamination after applying all cuts to be $\sim 10\%$ at lowest momentum 1.4 GeV/c, and $\sim 2\%$ in the momentum range $P_{\pi} = 3{-}4$ GeV/c. The uncertainty associated with pion decay is estimated to be $\leq$1%.

Pion Absorption: Some pions are lost due to nuclear interactions in the materials that the particles pass through on their way from the target to the HMS detector hut. Pions lost in hadronic interactions are largely due to absorption and large angle scattering, resulting in pions that do not strike all detectors required to form a trigger. The transmission of pions through the spectrometer is defined as the fraction of pions that do not interact with any of the materials.

The calculation of the pion transmission through the materials is determined by the choice of pion-nucleus cross section. In particular, the total cross section, which is defined as the sum of all hadronic interactions, represents an underestimate of the transmission. This can be explained in terms of the contribution of the individual pieces to the effective loss of pions. Elastic scattering is peaked in the forward direction (small angles), so that a large fraction of the elastically scattered pions are expected to still produce a valid pion event. In addition, inelastic scattering does not necessarily correspond to an invalid trigger. On the other hand, a pion that is truly "absorbed" will clearly not result in a trigger. Therefore, the transmission is calculated from the reaction cross section which includes all hadronic interactions except for elastic scattering ($\sigma_{reac} = \sigma_{absorption} + \sigma_{inelastic}$). The reaction cross section is approximately the average of the total and absorption cross sections and the uncertainty on the transmission can be estimated from these two limiting cases. At all kinematic settings of E00-108, the pion absorption was estimated to be below $1-2$ %.

TABLE VIII: Fraction of K^+ relative to π^+ (in %) for hydrogen and deuterium targets, for two different cuts on the number of photoelectrons (N_{pe}) in the aerogel detector.

	$(K^+/\pi^+)_H$		$(K^+/\pi^+)_D$	
z	$N_{pe}>0$	$N_{pe}>1$	$N_{pe}>0$	$N_{pe}>1$
0.97	9.2	8.9	11.4	10.4
0.85	5.6	5.2	7.2	6.3
0.74	2.7	2.0	3.5	2.5
0.64	0.2	0.1	0.3	0.1

TABLE IX: Kaon contamination (%) in hydrogen and deuterium data at $N_{pe} > 1$ cut on aerogel. Estimations are based on linear fits (Eq. 10) of the data from Table VIII

P_{HMS} GeV/c	z	K^+(H)	K^-(H)	K^+(D)	K^-(D)
3.703	0.97	9.3±0.9	0.6±0.2	10.9±0.9	0.9±0.2
3.222	0.85	7.6±0.5	0.4±0.3	8.9±0.5	-0.2±0.3
2.803	0.74	4.7±0.6	0.3±0.4	5.6±0.7	0.5±0.3
2.439	0.64	3.3±1.1	-0.1±0.2	3.6±1.3	0.1±0.1

Kaon contamination: For low momentum settings ($P_{HMS} < 2.4$ GeV/c), which is the case for our x-scan and P_t-scan data, kaon contamination is negligible. At these momenta the real e-K coincidence peak will be well outside the e-π coincidence peak, so the kaons are eliminated by the coincidence timing cut. In addition the HMS aerogel Čerenkov detector can be used for separation of pions from kaons. For kinematics with pion momenta above 2.4 GeV/c, a correction was made to remove kaons from the pion sample. To estimate kaon contamination, the coincidence timing distribution was analyzed for z-scan data. It was assumed that the "real" coincidence peak is a sum of π+K, therefore this spectrum was fitted with a sum of two Gaussian distributions [86].

The summary on kaon contamination is presented in Tables VIII and IX. The contamination at negative polarity was found to be very small. For positive polarity the worst case (about 10% contamination) was found at $z > 0.85$, but a more typical contamination is less than 2%

Kaon contamination from the actual data was corrected for as:

$$Y_{exp}^{corr} = Y_{exp} \times (1 - R_k), \tag{10}$$

where

$$\begin{aligned} R_k^H &= 0.265 \times (z - 0.63) \\ R_k^D &= 0.294 \times (z - 0.63) \end{aligned} \tag{11}$$

for hydrogen and deuterium targets.

Tracking Efficiency and Multiple Tracks: The tracking algorithm performs a χ^2 minimization by fitting a straight line through both drift chambers. The tracking efficiency is defined as the ratio of events that should have passed through the drift chambers and the number of events for which a track was found. The fraction of

events that should have passed through the drift chambers is defined by a requirement on hits in a fiducial area composed of a particular set of scintillator paddles. The efficiency depends on both the drift chamber hit efficiency and the tracking algorithm finding a track.

On average, the typical tracking efficiencies for pions in the HMS are better than 95% in most cases and are often better when electrons are detected in coincidence in SOS. At both positive and negative polarities of the HMS, and hydrogen and deuterium targets, during data taking the beam current was optimized to keep the HMS rate below 500−600 kHz. This helps to minimize the well-known negative impact of multiple hits on track reconstruction in HMS. In many cases the events with more than 15 hits in both chambers are caused by projectiles scraping the edge of one of the magnets and causing a shower of particles, hence multiple hits in the drift chambers. Examination of such events and data taken with high rates in HMS and/or SOS spectrometers revealed that sometimes the tracking code picks as the "best" among multiple track candidates a track that is not what a user looking at the event display would have picked. To eliminate this problem a new code was written that uses selection criteria different from the one track criteria [86].

With the new code the resulting tracking efficiencies in HMS and SOS are on the level of 97±0.1% and 98±0.4% respectively. (With the improved "pruning" algorithm we gain about 2-3% useful tracks). The difference between HMS and SOS mainly reflects the difference in incident count rates.

Coincidence and Čerenkov detector blocking: Another source of event loss is connected with coincidence and Čerenkov detector blocking effects. The coincidence time is determined by a clock that starts when an HMS signal arrives and stops when the SOS signal arrives. Two effects can cause the coincidence timing for good events to fail. In the first case, a random SOS single arriving before the coincident particle can stop the clock too early, effectively blocking the coincidence. A cut on the coincidence time will largely remove these events. The second effect is that a late SOS trigger can confuse the timing logic in such a way that the coincidence timing clock, which usually starts with the HMS and stops with the SOS, starts and stops with SOS ("retiming"). Wrongly timed events appear at lower (coincidence blocking) and higher (retiming) TDC channel numbers.

The coincidence blocking factor was calculated for a number of runs taken at different trigger rates using HMS-SOS raw (not corrected for pathlength) coincidence time (TDC's) spectra. We found that the coincidence blocking correction, k_{coin}, depends nearly linearly on the rate of the pretrigger, 5-40 kHz for the case of the electron spectrometer, the SOS. The coincidence blocking correction was then parameterized in terms of

$$k_{coin} = 1 - \alpha N_{strig}, \tag{12}$$

where $\alpha \approx 2.218 \times 10^{-5}$ and N_{strig} is the SOS trigger rate (in Hz). This correction for our coincidence time window of 120 ns was up to 4.5%, with an uncertainty of ∼0.1%.

The HMS gas Čerenkov detector is used for electron rejection in the π^- production case. The effective time window is given by the Čerenkov detector ADC "gate" and is approximately 100 ns wide. The loss of pions due to Čerenkov-detector blocking is due to electrons passing through the detector after the first particle (pion), but within the effective ADC gate window. In this situation, the signal from the electron will be associated with the original pion trigger and the pion event will be mis-identified as an electron. Such mis-identified pions are eliminated due to analysis cuts, so that the electron event effectively blocks the HMS Čerenkov detector for good pion events. The number of pions lost due to the Čerenkov detector blocking depends only on the rate of electrons into the spectrometer and does not depend strongly on variations in run to run characteristics. Therefore, we have used a small sample of measurements to determine the size of the correction for given kinematics, and for electron rates in the range of 20-500 kHz parameterized it in a functional form:

$$\tau_{cer} = 1 - 1.6 \times 10^{-7} \times \frac{N_{hecl}}{T_{run}}, \tag{13}$$

where N_{hecl} is the clean electron trigger (ELCLEAN) counts, defined by high level cuts on calorimeter and Čerenkov detector, and T_{run} is the duration of the run (in seconds). Čerenkov-detector blocking effect was on the level of ∼2% at 100 kHz, and reached up to ∼6% at 400 kHz, with a systematic error less than 1%. The uncertainty in the HMS Čerenkov detector blocking correction is largely attributed to the uncertainty in the Čerenkov detector timing window. In particular the effective Čerenkov detector gate width can be slightly larger than the measured ADC gate (≈100 ns). While the ADC gate is fixed, the Čerenkov detector signal itself has some width and the overlap determines an effective gate width.

Computer Dead Time: The computer dead time strongly depends on the trigger rate and experimentally is directly measured by scalers that record the number of triggers (N_{trig}) and pretriggers ($N_{pretrig}$). Since pretriggers are generated for each particle, and triggers are only read out for those events for which the Trigger Supervisor is not busy, the computer live time is $N_{trig}/N_{pretrig}$.

The computer dead time varied from a few percent at low rates to up 30% at trigger rate ∼2 kHz. The uncertainty in the computer live time measurement is estimated by the deviation of the measured value from the value calculated from the total rate. The resulting uncertainty is ∼ 0.2%. The electronic dead time was always ≤ 1% and often negligible.

For the E00-108 experiment, the computer and electronic live time corrections are applied run-by-run. More details of the analysis and corrections can be found in Ref. [86, 87].

Other corrections: From a measurement detecting positrons in SOS in coincidence with pions in HMS, we

found the background originating from π^0 production and its subsequent decay into two photons and then electron-positron pairs, or $e^+e^-\gamma$ directly, negligible. In addition, a small $\sim 2\%$ correction was made to the deuterium data to account for a small Final-State Interaction effect of the pions traversing the deuterium nucleus [88].

B. Model Cross Section and Monte Carlo Simulations

We added the possibility of semi-inclusive pion electroproduction to the general Hall C Monte Carlo package SIMC [89], using Eq. (1). The CTEQ5 next-to-leading-order (NLO) parton distribution functions were used to parametrize $q_i(x,Q^2)$ [90], and the fragmentation function parameterization for $D^+_{q_i\to\pi}(z,Q^2) + D^-_{q_i\to\pi}(z,Q^2)$, with D^+ (D^-) the favored (unfavored) fragmentation function, from Binnewies *et al.* [18]. The remaining unknowns are the ratio of D^-/D^+, the slope b of the P_t dependence, and the parameters A and B describing the ϕ dependence. Both the D^-/D^+ ratio [91] and the b-value [92] are taken from HERMES analysis. The latter is chosen for consistency with the comparisons shown in our earlier publication [13], but closely coincides with the averaged value for all data. We will study the detailed P_t-dependence of our data later on in Section VIIF.

When analyzing our data as a function of P_t, we found that the Q^2-dependence of the cross sections needed to be altered slightly from the factorized high-energy expectation [93] to obtain a smooth P_t dependence. This is not too surprising, as the (low) energies of our semi-inclusive pion production measurements are beyond the region where the BKK fragmentation functions were shown to describe existing data. Hence, we introduced an additional Q^2-dependent multiplicative term in the model cross section in the form

$$F(Q^2) = 1 + C_1 \cdot \ln(Q^2) + \frac{C_2}{Q^2} + \frac{C_3}{Q^4}. \qquad (14)$$

The parameters C_1, C_2 and C_3 were adjusted in such a way that the calculated yields from the SIMC simulation match the experimental data. To accomplish this, the ratio of experimental and SIMC yields were calculated in a number of Q^2 bins, and the model cross section was iterated until the ratios approach unity. A variety of fits, with different combinations of data included, more complicated fit functions (including ϕ-dependent terms with additional binning in ϕ and P_t) rendered parameters C_i that remained reasonably stable, within $\pm 10-20\%$. As average "best values" for the fit parameters, we adopted $C_1 = 0.889$, $C_2 =$ -2.902 and $C_3 =$3.050. Recall that for most of the cross section results (at $P_t \approx 0.05$ GeV/c) we neglected the ϕ-dependence and kept the parameters A and B at 0, in accordance with both theoretical expectations (discussed in subsection III B), and our own findings (see subsection VII A).

TABLE X: Corrections and systematic uncertainties.

Source of correction	Range (%)	Systematics (%)
Detector inefficiencies	5-10	1-2
Target wall contribution	2-3	1.0
Accidentals	10-20	1-2
Pion absorption	1-2	1.0
Pion decay	2-10	1.0
Kaon contamination	0.2-2.0	0.5 ($z < 0.7$)
Radiative corrections	5-10	1-2
Exclusive tail	5-15	0.5-2.5 ($z < 0.8$)
Pions from diffractive ρ	5-15	0.5-2.5
Computer Dead Time	5-25	0.2
Coincidence blocking	1-4.5	0.1
Čerenkov detector blocking	2-4	$\leq$1
Other corrections	1-2	1.0
Total	15-40	3.5-7.5

VI. SYSTEMATIC UNCERTAINTIES

As part of the analysis, several systematic studies were performed on the data to verify that the measured cross sections and ratios are not biased by the detector, event selection and background correction effects. The level of corrections applied to the experimental data and related systematic uncertainties are listed in Table X.

For absolute cross sections we have added all systematic uncertainties in quadrature. Note, that in practice the range of applied corrections and related systematic errors are slightly different for π^+ and π^-. For example, the Čerenkov blocking is clearly far larger for π^-. Part of the corrections (such as radiative, pion decay, detector inefficiencies) are nearly identical for π^+ and π^- and cancel in the ratios, hence related systematic uncertainties are much smaller for the ratios. Below we will discuss the most dominant sources of systematic uncertainties related with pions from the radiative tail from exclusive pion electroproduction and pions from the decay of diffractive ρ^o mesons.

A. Uncertainties related to the exclusive pion tail

The model used in SIMC for exclusive pion electroproduction mainly focused on parallel kinematics (with the outgoing pion along the direction of the virtual photon) for the purpose of understanding the z-scan data. To estimate the possible systematic error that arose from ignoring the LT and TT interference terms, and to test the absolute magnitude of the correction, we extracted simulated yields for the exclusive radiative tail calculated using our nominal, empirical parameterization as well as the MAID model.

Figures 5, 6 and 7 show the results of these simulations (MAID = red circles, SIMC= blue squares). The yields from each model [top panel] as well as the ratio between the two [bottom panel] are plotted versus θ_{pq}. While the two calculations differ in the absolute mag-

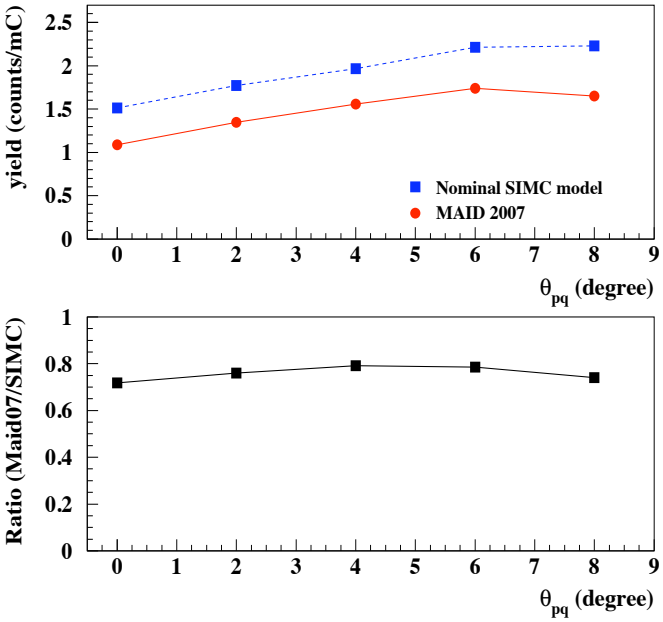

FIG. 5: (Color online) The exclusive radiative tail simulations for positive pions from deuterium using the nominal model cross section in SIMC described in the text. The top plot shows the total simulated yield from exclusive radiative events vs. the angle between the outgoing pion and the virtual photon. All points are at a fixed $z = 0.55$. For comparison, the yield using the MAID model (which has limited validity for $W > 2$ GeV) is also shown. The bottom panel shows the ratio of exclusive yields from both models.

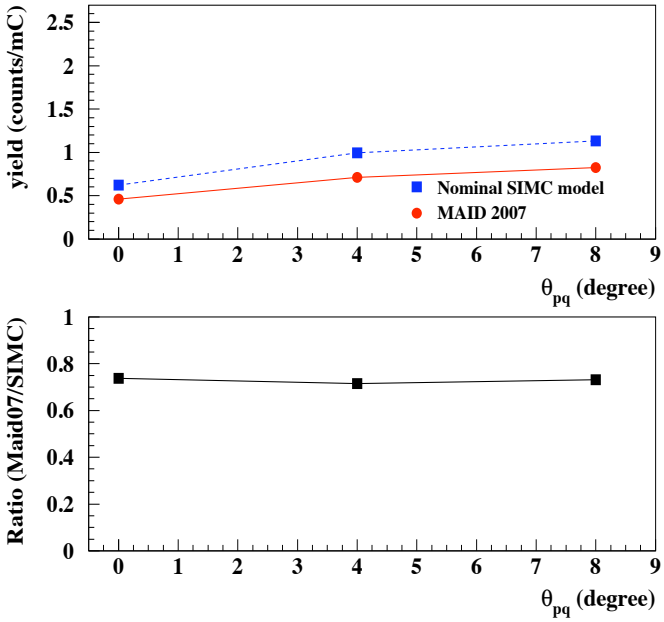

FIG. 6: (Color online) The exclusive radiative tail simulations for negative pions from deuterium (as in Fig. 5).

nitude of the exclusive yield, the ratio of yields shows little dependence on the outgoing pion angle. This suggests that the choice to ignore the interference terms in the SIMC parameterization had minimal effect (the contribution from the interference terms should increase at larger pion angles) over the region studied.

The effective W at the vertex for events that contribute to these yields is around 1.9 GeV (on average) so the empirical parameterization in SIMC, which agrees well with the JLab data at $W = 1.95$ GeV, should be more appropriate. Half of the difference between the two results was used as an estimate of the systematic uncertainty for the contribution of radiative exclusive events to the semi–inclusive yield.

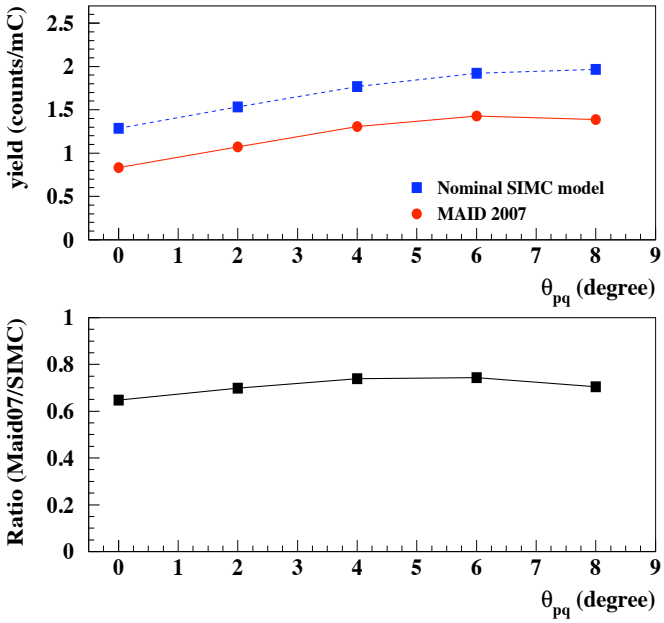

FIG. 7: (Color online) The exclusive radiative tail simulations for positive pions from hydrogen (as in Fig. 5).

B. Uncertainties related to events from diffractive ρ production

This uncertainty is related to the choice of the parameterization for the ρ^o cross sections. As mentioned, we used cross section based on the PYTHIA [82] generator with modifications as implemented by the HERMES collaboration [83] and additional modifications to improve agreement with CLAS data [84]. To estimate systematic uncertainties related to the diffractive ρ subtraction, all calculations were repeated with slightly (∼10%) different values of the parameters. Thus it was found that the diffractive ρ subtraction contributes a systematic uncertainty of up to $\approx 2.5\%$.

C. Other sources of systematic uncertainties

The systematic uncertainties due to normalization, target thickness, computer and electronic dead time, beam charge measurement, beam energy and spectrometer kinematics combine to approximately 2%. We note that targets and spectrometer polarity were exchanged frequently in this experiment, without noticeable effects.

The overall systematic uncertainty due to spectrometer acceptances is estimated to be $\leq 1\%$. This is because the spectrometers have a sufficient wide vertex length acceptance to view a 4 cm extended target with limited acceptance losses, given that the SOS spectrometer angle was limited to relatively forward angles, and that the particles of interest cover a central region of the SOS momentum acceptance only. The HMS spectrometer has a 10 cm uniform vertex length acceptance, and was used in the E00-108 experiment to view a 4 cm extended target at angles of 20 degrees or less. Hence, the HMS has full acceptance.

It was verified that the level of changes in our results due to variation of the values of PID cuts in the analysis slightly varies from case to case but is less than 1-2%. These variations are within the systematic uncertainties assigned to the detector efficiencies, and so are not taken as a separate additional source of uncertainty.

VII. EXPERIMENTAL RESULTS

Some of the results have been described in two previous papers [13, 94]. In the first, we observed for the first time the quark-hadron duality phenomenon in pion electroproduction, and the relation with a precocious low-energy factorization approach in semi-inclusive deep inelastic scattering. We quantified the latter by constructing several ratios of pion electroproduction cross sections off proton and deuteron targets, and found the ratio of favored to unfavored fragmentation functions to closely resemble that of high-energy reactions, up to about $z = 0.7$ or missing mass $M_x^2 > 2.5$ GeV^2 or so. In the second, we studied the transverse momentum dependence of semi-inclusive pion production, and found the dependence from the deuteron target to be slightly shallower than from the proton. In the context of a simple model, we related these measurements to the initial transverse momentum widths of down and up quarks, and the transverse momentum widths of favored and unfavored fragmentation functions. The results presented here supersede those of Ref. [94], which were for reduced statistics and improper application of some corrections.

In this article, we will present our full results in terms of cross sections and ratios for semi-inclusive charged-pion electroproduction off proton and deuteron targets, and relate the findings to the Quark-Parton Model expectations, further highlighting the onset of a precocious high-energy factorized parton model description. However, for completeness we will start with a short Section recapitulating two relevant findings of the previous publications.

A. The azimuthal angle ϕ and z dependence of the cross sections

In the E00-108 experiment, the average value of the angle ϕ is correlated with P_t, see Fig. 4 (the effect is tabulated in [94]). However, we will initially show results that have only small average value $P_t \approx 0.05$ GeV/c, to later on come back to the results as a function of P_t, including those for P_t up to 0.45 GeV/c, in a separate Section.

For the results at low P_t, one expects small to negligible contribution from the interference terms A and B in Eq. 1. We found no statistically significant difference between the results for π^+ or π^-, or proton or deuteron targets [95], and therefore combined all four cases together. Taking the systematic uncertainties of approximately 0.03 into account, we find values of A and B close to zero, with no noticeable x or z dependence. When averaged over all data, we find A = 0.02 $\pm$ 0.02 and B = -0.04 $\pm$0.02 at $P_t \approx 0.05$ GeV/c. Folding this back into Eq. 1, we can neglect the azimuthal-angle dependent corrections to the cross section and ratio results presented in the next Sections. The small values of A and B at small P_t for SIDIS kinematics are consistent with the expectations from kinematic shifts due to parton motion as described by Cahn [58] and Levelt-Mulders [59].

Since the bulk of our data is taken at low $P_t = 0.05$ GeV/c, we will neglect any ϕ-dependence and assume A = B = 0 until we explicitly revisit the P_t dependence of the measured cross sections and ratios later on.

In our first publication [13] we compared the measured ^{1,2}H(e,e$'\pi^{\pm}$)X cross sections as a function of z (at $x = 0.32$) with the results of a parton model calculation assuming CTEQ5M Parton Distribution Functions (PDFs) at Next-to-Leading Order [90] and the parameterized Fragmentation Functions (FFs) of Binnewies, Kniehl and Kramer (BKK) [18]. The ratio of unfavored to favored fragmentation functions D^-/D^+, and the slope b-values of the P_t dependences of the cross sections were taken from HERMES analysis [91, 92]. We found excellent agreement between data and Monte Carlo for $z < 0.65$, but striking deviations around $z = 0.8$. Within our kinematics (at $P_t \sim 0$), M_x^2 is almost directly related to z, as $M_x^2 = M_p^2 + Q^2(1/x - 1)(1 - z)$. Hence, we attributed the large "rise" in the data with respect to the simulation at $z > 0.8$ to the $N - \Delta(1232)$ region. Indeed, if one considers a ^{1}H(e,e$'\pi^-$)X spectrum as function of missing mass of the residual system X, one sees only one prominent resonance region, the $N - \Delta$ region. Apparently, above $M_x^2 \approx 2.5$ GeV^2, there are already sufficient resonances to render a spectrum mimicking the smooth z-dependence as expected according to the factorization ansatz of Eq. (1).

Much of the data shown later on as function of x, Q^2

and P_t, will be centered around $z = 0.55$, so well within the region where effects due to the N-Δ transition can be neglected, and excellent agreement was found between the low-energy pion electroproduction data and high-energy parton model expectations. We do note that this $z < 0.7$, or $M_x^2 > 2.5$ GeV^2 cut, corresponds to the prediction of Close and Isgur where duality and low-energy factorization would become valid [12, 27].

B. The x- and Q^2-dependence of the cross sections

At a fixed value $z = 0.55$, well within the range where we found excellent agreement between our cross section data and a naive high-energy ansatz in terms of next-to-leading-order (NLO) parton distributions (PDFs) convoluted with the BKK fragmentation functions (FFs), we will now study the x- and Q^2-dependence of the $^{1,2}H(e,e'\pi^{\pm})$X cross sections.

We studied the x-dependence in the range $0.2 \leq x \leq 0.6$ by varying the angle of the scattered electron, while keeping the beam energy and the virtual photon energy ($\nu \approx 3.9$ GeV) fixed. An additional advantage of this choice of z and ν is that the corresponding outgoing pion momentum is larger than 2 GeV/c, well in the region where the $\pi - N$ cross sections behave smoothly such that final-state interactions do not overly complicate interpretation of the pion yields. Restricting the kinematics to such large pion momenta permits to neglect possible differences in π^+ and π^- rescattering. In a simple Glauber calculation we estimated the total pion absorption correction due to rescattering to be 2% for a deuterium target, and the difference between π^+ and π^- to be less than 1%. We apply the 2% deuteron correction for all ^{2}H data, and assume a constant $b = 4.66$ (GeV/c)$^{-2}$ to describe the P_t dependence, somewhat different from what we will derive from the specific P_t-dependent measurements later on. Even though this does not affect the cross sections represented, it does impact the overall agreement with the parton-model calculations, where b comes in as an overall normalization. The choice $b = 4.66$ (GeV/c)$^{-2}$ is chosen in these figures for consistency with the comparisons shown in our earlier publication [13]. We note that this choice is also consistent with the HERMES findings.

We present in Figs. 8 and 9 a selection of differential cross sections for the $^1H(e,e'\pi^{\pm})$X and $^2H(e,e'\pi^{\pm})$X reactions, respectively, at low and high "x_{set}" values of the experiment (by this we mean the x value as calculated from the central spectrometer kinematics; using the finite spectrometer acceptances we present multiple x-bins). Since we vary the scattered electron angle, a variation in x_{set} (or x) likewise corresponds to a variation of Q^2_{set} (or Q^2). For $x_{set} = 0.32$, $Q^2_{set} = 2.30$ (GeV/c)^2 and for $x_{set} = 0.53$, $Q^2_{set} = 3.8$ (GeV/c)^2 cross sections are shown along with the model calculations. For simplicity, we have only considered CTEQ5M parton distributions at NLO [90] and the BKK [18] fragmentation functions, allowing for a slightly modified Q^2 dependence. The scope

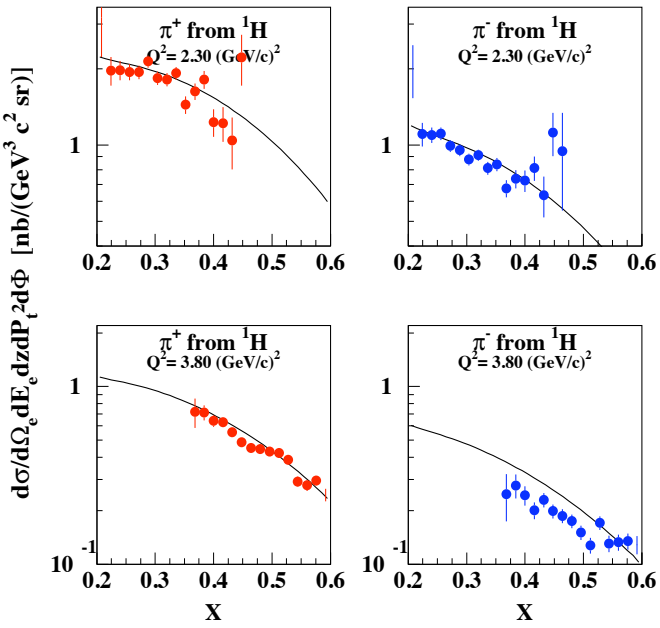

FIG. 8: (Color online) The ^{1}H(e,e$'\pi^+$)X (left) and ^{1}H(e,e$'\pi^-$)X (right) cross sections at $z = 0.55$ as a function of x, at $Q^2_{set} = 2.30$ (GeV/c)^2) (top) and at $Q^2_{set} = 3.80$ (GeV/c)^2) (bottom), respectively. Solid curves are parton model calculations. Solid symbols are data after events from diffractive ρ production are subtracted (see text).

of this work is to judge how well low-energy pion electroproduction cross sections (and ratios) compare with parton model expectations, and comparisons with other possibly more sophisticated model calculations is beyond this scope. We conclude that the x-dependence agrees reasonably well with the model calculations, but differences in the absolute magnitude of the cross section are apparent in certain cases.

Next, we want to compare the Q^2-dependence of the measured cross sections with the parton model expectations. However, as described we varied x by a change in the electron scattering angle, which correlates higher x with higher Q^2. A similar correlation exists within the finite spectrometer acceptances. Hence, we need to remove this correlation to present data as function of Q^2 only, at a fixed value of x. We found that $x = 0.40$ is the optimal value to choose, accessible for each of the five settings of the x-scan ($x_{set} = 0.26$, 0.32, 0.39, 0.46 and 0.53). The x-dependence of the parton model, determined from SIMC simulations over the experimental acceptance, was used to scale all data within one x-scan setting to $x = 0.40$. This was accomplished by using the ratios of the normalized yields between data and Monte Carlo for each Q^2_i bin: Y_i^{exp}/Y_i^{MC}. The cross sections of different x-scan settings were then corrected to $x = 0.40$ using these ratios and the corresponding model cross sections at $x = 0.40$.

The $^{1,2}H(e,e'\pi^{\pm})$X cross sections for all five settings of the x-scan are shown versus Q^2 in Fig. 10, bin-centered to

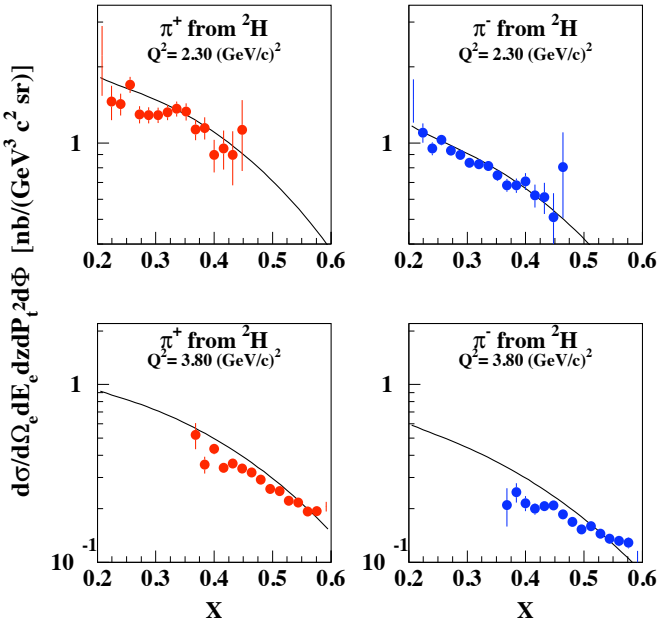

FIG. 9: (Color online) The ^{2}H(e,e′π^+)X (left) and ^{2}H(e,e′π^-)X (right) cross sections at $z = 0.55$ as a function of x, at $Q^2_{set} = 2.30$ (GeV/c)^2) (top) and at $Q^2_{set} = 3.80$ (GeV/c)^2) (bottom), respectively. Solid curves are parton model calculations. Solid symbols are data after events from diffractive ρ production are subtracted (see text).

x=0.40 with this technique. The curves are the parton model calculations, and describe the Q^2-dependence of our data remarkably well. Note that the Q^2-dependence is steeper than naively assumed for a swing in Q^2 from about 1.5 to 4.0 (GeV/c)^2, since these are cross sections, "bin-centered" to fixed $x = 0.40$, which induces trivial changes in for instance the beam energy and the resulting photon flux. Similarly, one can see that the calculated cross section drops very fast around $Q^2 = 4.0$ (GeV/c)^2, which reflects that one has reached the edge of what is kinematically possible with our experimental setup. As before, the solid symbols are the data after events from coherent diffractive ρ production are subtracted. Such corrections were estimated to be $\leq 10\%$ for these cross sections, and do not affect the conclusion that the Q^2-dependence of our data surprisingly conforms to the high-energy (quark-parton) expectations.

C. The z, x and Q^2 dependence of the cross sections ratios (π^+/π^- and D/H)

With the semi-inclusive pion electroproduction data at our relatively low energies closely resembling the high-energy parton model expectations, we now turn our attention to various ratios constructed from the data, in an effort to quantify the agreement with the quark-parton model. Especially the ratio of charged π^+ and π^- semi-inclusive electroproduction cross sections (or the ratio of their normalized yields, π^+/π^-) is a quantity relatively easy to measure accurately with focusing magnetic spectrometers. In contrast to a large-acceptance detector, the acceptance, reconstruction, and detection efficiencies for positively- and negatively-charged pions are very similar in a focusing magnetic spectrometer, allowing for precision comparisons.

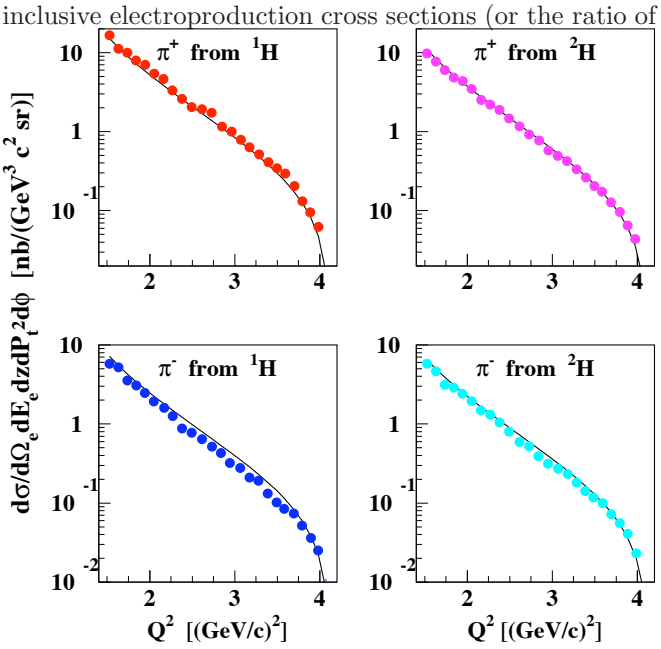

FIG. 10: (Color online) The ^{1,2}H(e,e′$\pi^\pm$)X cross sections at fixed values of $x = 0.40$ and $z = 0.55$, as a function of Q^2. The solid curves are the simple quark-parton model calculations following a high-energy factorized description. Solid symbols are data after events from diffractive ρ production are subtracted (see text).

With the assumptions of factorization, isospin symmetry and charge conjugation (and neglecting heavy quarks in the valence-quark region), the cross sections (or normalized yields) of $\pi^\pm$ production on protons and neutrons at fixed Q^2 can be presented as:

$$
\begin{aligned}
{\sigma_p}^{\pi^+}(x,z) &\propto 4u(x)D^+(z) + d(x)D^-(z) + 4\bar{u}(x)D^-(z) + \bar{d}(x)D^+(z) \\
{\sigma_p}^{\pi^-}(x,z) &\propto 4u(x)D^-(z) + d(x)D^+(z) + 4\bar{u}(x)D^+(z) + \bar{d}(x)D^-(z) \\
{\sigma_n}^{\pi^+}(x,z) &\propto 4d(x)D^+(z) + u(x)D^-(z) + 4\bar{d}(x)D^-(z) + \bar{u}(x)D^+(z) \\
{\sigma_n}^{\pi^-}(x,z) &\propto 4d(x)D^-(z) + u(x)D^+(z) + 4\bar{d}(x)D^+(z) + \bar{u}(x)D^-(z),
\end{aligned}
\tag{15}
$$

with D^+ and D^- the favored and unfavored fragmentation functions, respectively.

The ratio of charged pion production on proton and neutron will then be:

$$
\begin{aligned}
\frac{{\sigma_p}^{\pi^+}}{{\sigma_p}^{\pi^-}} &= \frac{4u(x)+\bar{d}(x)+(d(x)+4\bar{u}(x))\cdot\frac{D^-(x)}{D^+(x)}}{(4u(x)+\bar{d}(x))\cdot\frac{D^-(x)}{D^+(x)}+d(x)+4\bar{u}(x)} \\
\frac{{\sigma_n}^{\pi^+}}{{\sigma_n}^{\pi^-}} &= \frac{4d(x)+\bar{u}(x)+(u(x)+4\bar{d}(x))\cdot\frac{D^-(x)}{D^+(x)}}{(4d(x)+\bar{u}(x))\cdot\frac{D^-(x)}{D^+(x)}+u(x)+4\bar{d}(x)}.
\end{aligned}
\tag{16}
$$

It is obvious that the fragmentation functions do not completely cancel in the π^+/π^- and D/H ratios, and some z-dependence remains carried by the term D^-/D^+. However, in the ratio of charge-combined cross sections, such z-dependence will completely cancel. Some of those "super-ratios" were presented in our first publication [13], and showed validity of the factorization assumption up to $z \sim 0.65$: no z-dependence was found.

The π^+/π^- and D/H ratios versus z: Various ratios of cross sections of positively- and negatively-charged pions and proton and deuteron targets are shown as a function of z (at $x = 0.32$) in Figs. 11 and 12. Solid (open) circles and squares again represent the data after (before) events from diffractive ρ decay are subtracted. We also added existing data for the charged-pion production ratios from Cornell [97], with the solid and open triangles representing data at $Q^2 = 2.0$ (GeV/c)^2 and $x = 0.24$, and $Q^2 = 4.0$ (GeV/c)^2 and $x = 0.50$, respectively. The solid line is again the simple quark-parton model calculation.

The π^+/π^- ratio as measured from the proton target is larger than those reported by HERMES [98], but agrees well with the older Cornell data [97], and is consistent (but not equal) to the rise in z as expected from the quark-parton model calculation up to $z \approx 0.6$. At values of $0.65 < z < 0.85$, the ratio decreases because the $\pi^-\triangle^{++}$ cross section is larger than the $\pi^+\triangle^o$ one. The sharp rise of the ratio at $z > 0.85$ is due to exclusive π^+ production. On the other hand, the π^+/π^- ratio measured on the deuteron reproduces the expected rise from the quark-parton model calculation very well. The data seem to continue the rising trend for $z > 0.7$, into the region where we noticed effects from the $N - \Delta$ transition before.

In our previous article [13] this was explained within the SU(6) symmetric quark model, which essentially removes the effect of resonance transitions on this particular ratio, which is inversely proportional to the ratio of unfavored to favored fragmentation functions: $D^-/D^+ = (4 - r)/(4r - 1)$, with r the ratio of π^+ over π^- yields off a deuteron target. The observed z-dependence of the resulting D^-/D^+ ratio agreed very well with a fit by the HERMES collaboration of their data. In [13] it was also observed that the resulting D^-/D^+ ratio was independent of x, as it should be, and agreed quite well with previous HERMES and EMC data. For completeness and future use, we have added in this manuscript the D^-/D^+ ratios in tabular format in Table XI and XII. The columns represent the data before and after events from diffractive ρ decay are subtracted.

When expressed as a nuclear (deuteron over proton) ratio of positively-charged π^+ yields and negatively-charged π^- yields (see Fig. 12), the data show a relatively flat behavior as a function of z up to about $z = 0.7$, where the $N - \Delta$ transition comes in again. These ratios

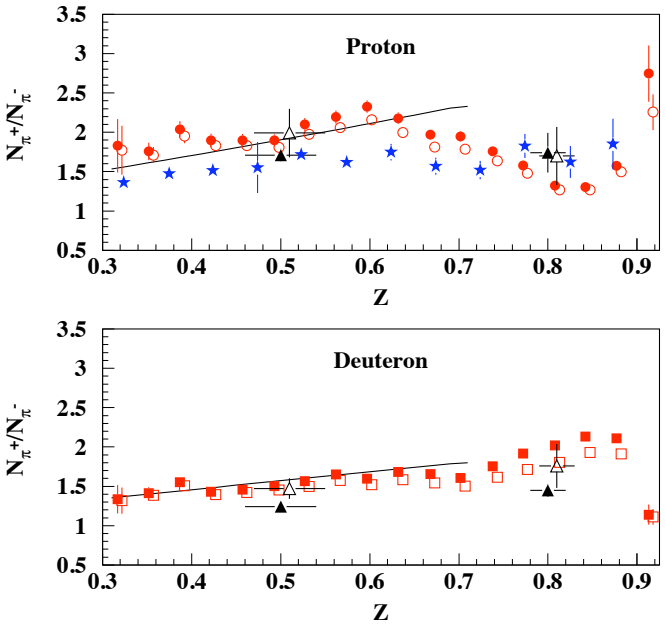

FIG. 11: (Color online) The ratio π^+/π^- for proton (top panel) and deuteron (bottom panel) targets as a function of z, at $x = 0.32$. Solid (open) circles and squares represent the data after (before) events from diffractive ρ decay are subtracted. Solid and open triangles represent existing Cornell data [97] at $Q^2 = 2.0$ (GeV/c)^2 and $x = 0.24$, and $Q^2 = 4.0$ (GeV/c)^2 and $x = 0.50$, respectively. Stars represent HERMES data [98] at average values of $\langle Q^2\rangle$=2.5 (GeV/c)^2, $\langle W^2\rangle$=28.6 GeV^2, $\langle\nu\rangle$=16.1 GeV and $\langle x\rangle$=0.082. The solid line is a naive quark-parton model calculation.

TABLE XI: The ratio of unfavored to favored fragmentation function D^-/D^+ as a function of z, at x=0.32, evaluated at leading order of α_s (neglecting strange quarks) from the deuterium data.

z	$D^-/D^+(after\ \rho)$	$D^-/D^+(before\ \rho)$
0.342	0.4620±0.0710	0.4620±0.0710
0.370	0.4196±0.0475	0.4449±0.0465
0.398	0.4838±0.0453	0.5126±0.0438
0.426	0.4764±0.0429	0.5087±0.0411
0.454	0.4575±0.0414	0.4940±0.0392
0.482	0.4425±0.0413	0.4837±0.0395
0.510	0.4059±0.0318	0.4530±0.0306
0.538	0.3635±0.0270	0.4134±0.0257
0.566	0.3699±0.0266	0.4288±0.0253
0.594	0.3638±0.0274	0.4280±0.0267
0.622	0.3448±0.0298	0.4124±0.0284
0.650	0.3157±0.0289	0.3853±0.0279
0.678	0.3587±0.0314	0.4376±0.0307
0.706	0.3934±0.0327	0.4800±0.0319
0.734	0.3137±0.0273	0.3889±0.0264
0.762	0.3164±0.0254	0.3911±0.0254
0.790	0.2738±0.0223	0.3375±0.0223
0.818	0.2625±0.0198	0.3177±0.0198
0.846	0.2380±0.0177	0.2808±0.0168
0.874	0.2294±0.0161	0.2607±0.0159
0.902	0.2423±0.0243	0.2555±0.0238
0.930	0.3025±0.0739	0.2944±0.0724

TABLE XII: The ratio of unfavored to favored fragmentation function D^-/D^+ as a function of x, at z=0.55, evaluated at leading order of α_s (neglecting strange quarks) from the deuterium data.

x	$D^-/D^+(after\ \rho)$	$D^-/D^+(before\ \rho)$
0.213	0.5048±0.0835	0.5682±0.0800
0.238	0.4272±0.0458	0.4789±0.0435
0.263	0.4008±0.0341	0.4472±0.0322
0.287	0.3939±0.0311	0.4361±0.0294
0.312	0.4049±0.0289	0.4446±0.0277
0.338	0.4278±0.0285	0.4660±0.0274
0.363	0.3334±0.0252	0.3631±0.0242
0.388	0.3690±0.0263	0.3987±0.0253
0.413	0.3476±0.0262	0.3732±0.0249
0.438	0.3914±0.0298	0.4177±0.0287
0.463	0.3907±0.0320	0.4142±0.0310
0.488	0.4198±0.0362	0.4420±0.0349
0.513	0.4436±0.0403	0.4546±0.0395
0.538	0.4202±0.0454	0.4385±0.0440
0.562	0.4721±0.0581	0.4890±0.0572
0.588	0.3533±0.0553	0.3668±0.0539

appear in reasonable agreement with the quark-parton model calculations.

The x- and Q^2-dependence of the π^+/π^- and D/H ratios: Given that the z-dependence of our low-energy semi-inclusive pion electroproduction data show a smooth behavior up to $z = 0.7$, in reasonable agreement with the quark-parton model expectations, we now turn to the x and Q^2 dependence of the various ratios. In Figs. 13 and 14 we show the ratio of positively- to negatively-charged pions versus x and Q^2, respectively,

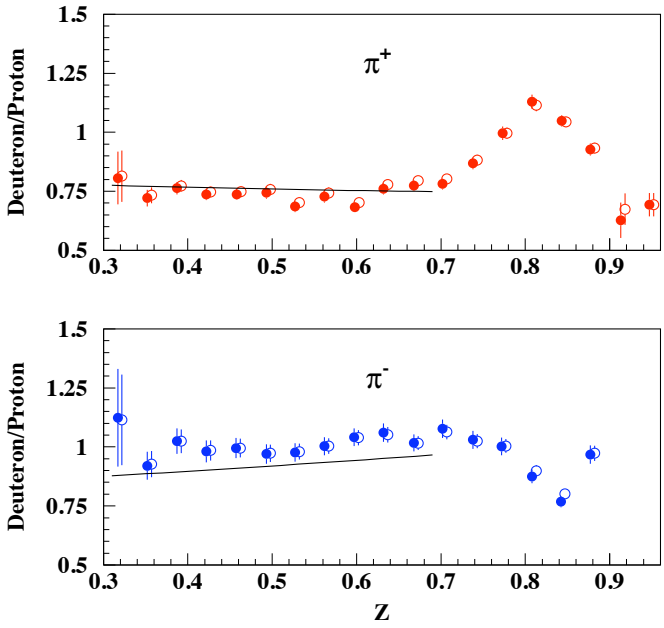

FIG. 12: (Color online) The deuteron over proton (D/H) yield ratio for π^+ mesons (top panel) and π^- mesons (bottom panel), as a function of z at fixed $x = 0.32$. Solid (open) symbols represent the new data after (before) events from diffractive ρ decay are subtracted. The solid lines are the quark-parton model expectations, plotted up to $z = 0.7$ where effects from the $N - \Delta$ transition may enter the ratios.

for both proton and deuteron targets. As before, solid (open) circles and squares are the data after (before) corrections are made to subtract pions originating from diffractive ρ decay. The Q^2 dependence of the deuteron to proton ratio for ρ° production was studied by the HERMES collaboration [96]. We have also added existing data in Fig. 13 from Cornell [97]. Solid and open triangles represent data at $x = 0.24$ and $Q^2 = 2.0$ (GeV/c)^2, and at $x = 0.50$ and $Q^2 = 4.0$ (GeV/c)^2. As can be seen, the Cornell data are in good agreement with our data. The positively- to negatively-charged pion ratios are also in surprisingly good agreement with the quark-parton model prediction.

The Q^2 dependence of the ratios was extracted by using the π^+ and π^- production cross sections at $x = 0.26$, 0.32, 0.39, 0.46 and 0.53, and "bin-centering" these cross sections, and thus their ratios, as before, to one common value of $x = 0.4$. This was done by using the hadron part of the model cross section in SIMC. The correction was checked by running SIMC and taking cross section ratios for proton targets at the five x-scan central settings. The size of the applied corrections amounts to $\sim 15\%$ maximum for the proton target, and is always below 10% for the deuteron target.

The results, again at a value of $z = 0.55$, are shown in Fig. 14. The Q^2 dependence of these ratios is in very good agreement with the quark-parton model expectations, indicated by the solid curve. This teaches that

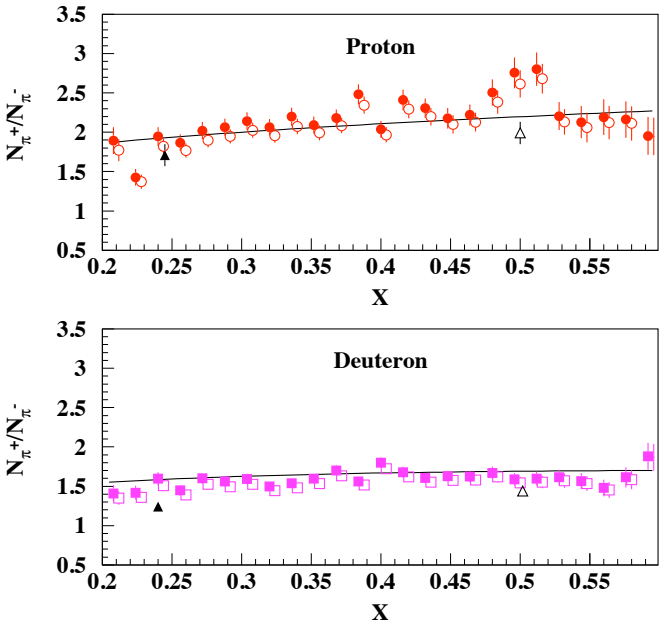

FIG. 13: (Color online) Ratio π^+/π^- for proton (top panel) and deuteron (bottom panel) targets as a function of x at $z = 0.55$. Solid (open) circles and squares are our data after (before) events from diffractive ρ decay are subtracted. Solid and open triangle symbols are Cornell data [97] at Q^2=2.0 (GeV/c)^2 and $x = 0.24$, and Q^2=4.0 (GeV/c)^2 and $x = 0.50$. The solid lines are the quark-parton model expectation.

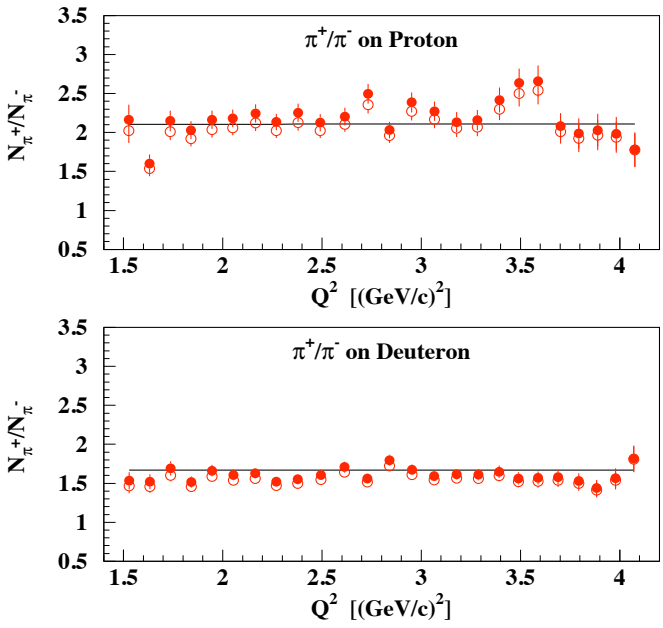

FIG. 14: (Color online) The ratio π^+/π^- for proton and deuteron targets as a function of Q^2 for $x = 0.4$ and $z = 0.55$. Solid (open) symbols are the ratios after (before) yields from diffractive ρ decay are subtracted. The solid lines are the simple quark-parton model expectations.

whereas the Q^2-dependence of the measured pion electroprodution cross sections is in reasonable, but not excellent, agreement with the quark-parton model expectations, as shown in Fig. 10, any spurious or higher-twist-related Q^2-dependence get completely absorbed in ratios (or have an origin in the x-dependence of such ratios, as there is a strong kinematical correlation between x and Q^2 within the E00-108 experimental setup). This is good news for low-energy access to quark-parton model physics in semi-inclusive meson electroproduction.

Lastly, we show in Figs. 15 and 16 the deuteron over proton ratios for π^+ and π^- electroproduction, as a function of x and Q^2, respectively. These nuclear D/H ratios are at a common $z = 0.55$ again, and the solid curves shown correspond as before to the quark-parton model expectations.

The conclusions from these nuclear D/H ratios are not unexpected. The dependences on x and Q^2 from the quark-parton model is remarkably close to the data, again confirming for these ratios that higher-twist effects are small or nearly cancel in ratios. The absolute magnitudes of the ratios slightly differs from the quark-parton model estimates, which reflects the similar difference noted in Fig. 12. Most obvious is the nuclear D/H ratio for the π^- electroproduction case, where the data are some 10% higher than the calculated quark-parton model ratio. The origin of the discrepancy is not yet clear, but on the other hand the data are at a relatively large x of 0.4, where the parton distributions themselves start having noticeable uncertainties. The latter is investigated in more detail in the next section, by constructing direct ratios of the d and u valence quark ratios from the data.

D. The ratio of d/u valence quarks constructed from charged-pion yields

The cross section for $\pi^\pm$ production on a deuteron at fixed Q^2 can be presented, in similar format and under identical assumptions, as the sum of the pion cross sections of Eq. (15):

$$\begin{aligned} {\sigma_d}^{\pi^+}(x,z) &\propto (4D^+(z)+D^-(z))(u(x)+d(x))+ \\ &\quad (4D^-(z)+D^+(z))(\bar{u}(x)+\bar{d}(x)) \\ {\sigma_d}^{\pi^-}(x,z) &\propto (4D^-(z)+D^+(z))(u(x)+d(x))+ \\ &\quad (4D^+(z)+D^-(z))(\bar{u}(x)+\bar{d}(x)) \end{aligned} \quad (17)$$

The measured cross sections or yields for $\pi^\pm$ production on the proton and deuteron can in the quark-parton model be directly used to form relations in terms of the u_v and d_v valence quark distributions:

$$\begin{aligned} {\sigma_p}^{\pi^+} - {\sigma_p}^{\pi^-} &\propto (D^+ - D^-)(4u_v - d_v) \\ {\sigma_d}^{\pi^+} - {\sigma_d}^{\pi^-} &\approx ({\sigma_p}^{\pi^+} - {\sigma_p}^{\pi^-}) + ({\sigma_n}^{\pi^+} - {\sigma_n}^{\pi^-}) \\ &\propto (D^+ - D^-)(3u_v + 3d_v), \end{aligned} \quad (18)$$

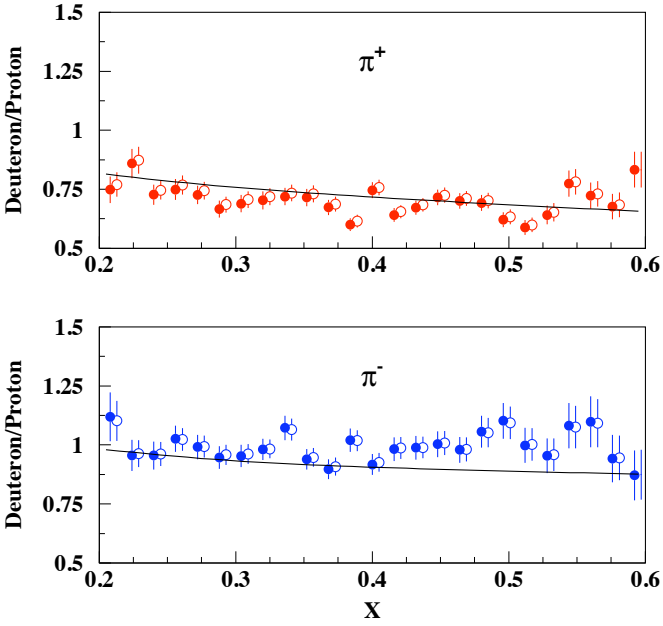

FIG. 15: (Color online) The ratio deuteron over proton for π^+ (top panel) and π^- (bottom) as a function of x at $z = 0.55$. The solid (open) symbols are the ratios after (before) yields from diffractive ρ decay are subtracted. The solid lines indicate the simple quark-parton model calculations.

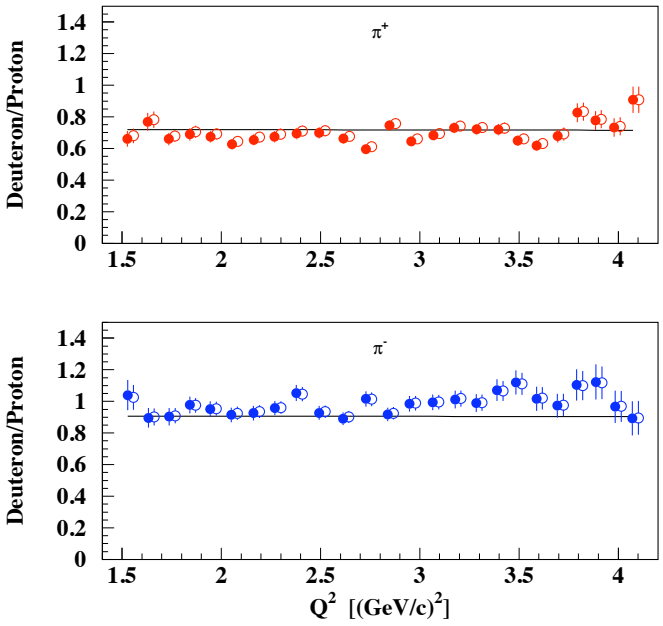

FIG. 16: (Color online) The ratio deuteron over proton for π^+ (top panel) and π^- (bottom) as a function of Q^2, at $x = 0.40$ and $z = 0.55$. The solid (open) symbols are the ratios after (before) yields from diffractive ρ decay are subtracted. The solid lines indicate the simple quark-parton model calculations.

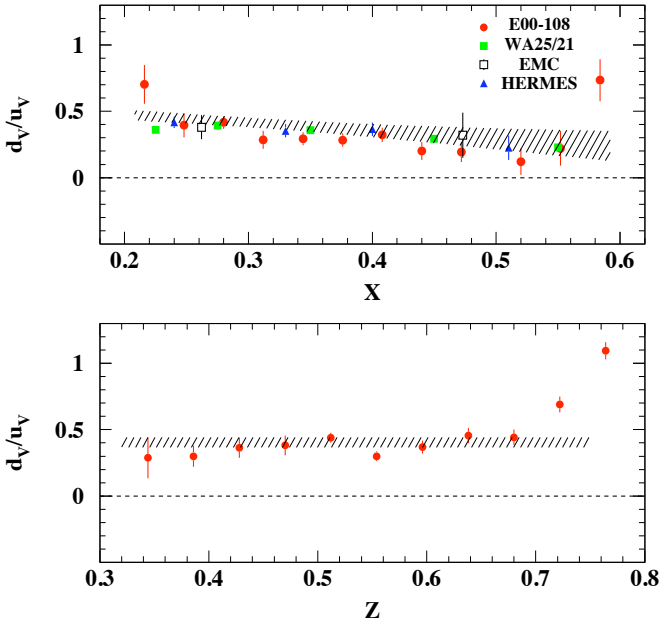

FIG. 17: (Color online) Top panel: The ratio of valence quarks d_v/u_v as a function of x at z=0.55. Solid circles are our data from E00-108 experiment (at $P_t \approx 0$) after events from ρ decay are subtracted. Solid and open squares represent data from WA-21/25 [99] and EMC [53]. Solid triangle symbols are HERMES data [55] integrated over the $0.2 < z < 0.7$ range. Bottom panel: The ratio of valence quarks d_v/u_v as a function of z at x=0.32. Solid circles are our data from E00-108 after events from diffractive ρ decay are subtracted. The shaded bands on both panels reflect the values of and uncertainties in this ratio using CTEQ parton distribution functions, based on Eq. 19 [90].

where $u_v = u - \bar{u}$, and $d_v = d - \bar{d}$. Of course, only the full parton distribution u (and d) is physical, but at intermediate to large x, $x > 0.3$, sea quark contributions are small and it is common to consider valence quark distributions only in this region.

The d_v/u_v ratio can be directly extracted from a specific combination of the measured proton and deuteron $\pi^\pm$ cross sections as follows:

$$R_{pd}^{-}(x) = \frac{\sigma_p^{\pi^+}(x,z) - \sigma_p^{\pi^-}(x,z)}{\sigma_d^{\pi^+}(x,z) - \sigma_d^{\pi^-}(x,z)} = \frac{4u_v(x) - d_v(x)}{3[u_v(x) + d_v(x)]}, \tag{19}$$

from which one finds

$$d_v/u_v = (4 - 3R_{pd}^{-})/(3R_{pd}^{-} + 1). \tag{20}$$

Studying the x and z (and P_t) dependences of R_{pd}^{-} and d_v/u_v thus provides an excellent test of the validity of the high-energy factorized view of the SIDIS process, and the various assumptions made.

The ratio d_v/u_v is shown in Fig. 17, both as a function of x at z=0.55 (top panel), and as a function of z at x=0.32 (bottom panel). The ratios extracted from our SIDIS data are also compared to WA-21/25 data

from neutrino and anti-neutrino deep inelastic scattering off proton targets (solid squares) [99], and to ratios extracted from forward hadron production data from the European Muon Collaboration (open squares) [53]. The shaded bands on both panels represent the values (including their present uncertainties) as calculated from Eq. 19 using CTEQ parton distribution functions [90].

The experimentally extracted ratios appear somewhat low as compared to the quark-parton model expectations using the CTEQ parton distributions, but possibly within uncertainties. For the results of the present experiment, one should not only take into account experimental systematic uncertainties, but also possible biases due to various assumptions in low-energy factorization and symmetry in fragmentation functions, etc. Nonetheless, the E00-108 data (at $P_t \approx 0$) are in good agreement with previous extractions of WA21/25 and EMC, with vastly different techniques.

The undershoot as compared to CTEQ parton distribution function expectations can be further investigated by investigating the dependence on z of the measured ratios at a fixed value of x (= 0.32). If isospin symmetry between favored (D^+) and unfavored (D^-) fragmentation functions of light quarks (u and d) and anti-quarks ($\bar{u}$ and $\bar{d}$) breaks down ($D_u^{\pi^+} \neq D_{\bar{u}}^{\pi^-} \neq D_d^{\pi^-} \neq D_{\bar{d}}^{\pi^+}$ and $D_u^{\pi^-} \neq D_{\bar{u}}^{\pi^+} \neq D_d^{\pi^+} \neq D_{\bar{d}}^{\pi^-}$), the ratios of Eq. 19 may contain additional z-dependent factors, related to asymmetries between the fragmentation functions. Thus, a dependence of the extracted "d_v/u_v ratio" on z will be a good indication for a breakdown of the symmetry assumptions, or of the factorized formalism. Indeed, one can witness in the bottom panel of Fig. 17 a sharp increase of the extracted d_v/u_v ratio at $z > 0.7$. This is likely not surprising as $z > 0.7$ corresponds in E00-108 kinematics to missing mass $M_x^2 < 2.5$ GeV^2), where *e.g.* the Δ- and higher-resonance contributions become dominant.

Below $z \approx 0.7$, the extracted d_v/u_v ratio is found to be reasonably independent of z, within the uncertainties of the data. On average, the data is somewhat low as compared to the quark-parton model expectations based upon CTEQ parton distribution functions, similar as was found in the x-dependence of this ratio. As a reminder, the data presented in Fig. 17 are at an average low $P_t \sim 0.05$ GeV/c; we will revisit any possible P_t dependence of the extracted ratio later on.

Even though the extracted d_v/u_v ratios from the E00-108 experiment tend to undershoot the expectations based upon CTEQ6 parton distributions, the agreement with the existing WA21/25 and EMC data is good, and possibly points to the applicability of the assumed factorization and access to the quark-parton model in relatively low-energy SIDIS data. This is consistent with our earlier findings in Ref. [13].

E. Nuclear Al/D ratios

We have also analyzed the pion production ratio from aluminum to deuterium targets, Al/D, by using the data from the "dummy" target cells. The nuclear EMC effect, the modification of the (inclusive) nuclear structure functions as compared to those of the free nucleon, was originally a revelation and firmly injected the subject of quarks into nuclear physics. In the valence quark region, a linear decrease in the nuclear ratio of structure functions (typically A/D) of about unity at $x = 0.3$ to a maximum depletion of 10-20% around $x = 0.7$ has been found. For medium to heavy nuclei, $A > 12$, the effect can be well described by either an atomic mass number $A^{-1/3}$ or nuclear density ρ dependence.

In semi-inclusive pion production, nuclear effects are more complicated, because in addition to influencing the electron-quark scattering part, they can affect the quark-hadron fragmentation process. For the purpose of the present discussion, we assume that the nuclear effects on parton distributions and fragmentation functions simply factorize. This has by no way been based on rigorous experimental verification.

Experimental results on semi-inclusive leptoproduction of hadrons from nuclei are usually presented in terms of multiplicity ratios between nuclear (A) and deuteron (D) targets as a function of z and ν:

$$R_A^h = \frac{1}{N_A^{DIS}} \frac{dN_A^h}{dz} \Big/ \frac{1}{N_D^{DIS}} \frac{dN_D^h}{dz} \approx \frac{dN_A^h}{dz} \Big/ \frac{dN_D^h}{dz}, \quad (21)$$

where the latter applies, if one can ignore EMC-type effects, true for $x \sim$0.3. Using the factorized assumption and neglecting the nuclear EMC effect for now (we will return to the x-dependence in the nuclear ratios later on), we first constructed a nuclear attenuation from the ratios of the normalized yields,

$$R_A^h \approx \frac{dN_A^h}{dz} \Big/ \frac{dN_D^h}{dz} = \frac{Y_A^h}{Y_D^h}, \quad (22)$$

where Y_A^h and Y_D^h are the normalized yields of the electroproduced pions from aluminum nuclei and deuterium, respectively.

In Fig. 18 we present the ratio of the normalized pion electroproduction yields, Al/D, for both π^+ (solid circles) and π^- (solid squares) versus z, at fixed x=0.32. The general features of the data, a value of R below unity and decreasing with z, are similar to what has been observed in other experiments and which globally have been explained within various models (see, e.g., [100] and references therein). This applies even in the region of $z > 0.7$ where for both the deuteron target and the nearly-isoscalar aluminum target nucleon resonances come into play (which within the symmetric SU(6) quark model cancel out).

The x-dependences of the Al/D cross section ratio for both π^+ and π^-, at $z = 0.55$, are shown in Fig. 19. We

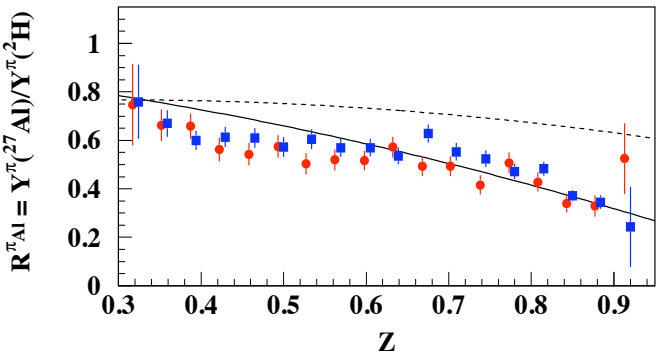

FIG. 18: (Color online) The ratio of aluminum over deuteron for both π^+ (circles) and π^- (squares) data as a function of z at $x = 0.32$. The dashed curve is a calculation based on the model for hadron formation of Bialas and Chmaj [101], with the hadron formation time inserted from a string tension model [102]. The solid curve is a prediction based on gluon radiation theory [103]. For the latter, we scaled between data for both ^{14}N and ^{64}Cu, assuming $(1 - R^h_A) \sim A^{1/3}$, and took the average value.

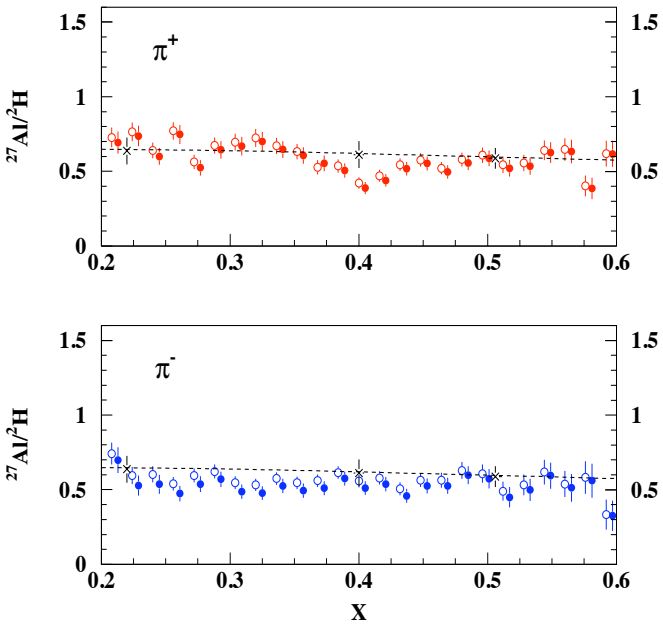

FIG. 19: (Color online) The ratio of aluminum over deuteron for π^+ (top panel) and π^- (bottom) as a function of x at $z = 0.55$. Solid (open) symbols are our data after (before) events from diffractive ρ production are subtracted. The cross symbols are Al/D data from the SLAC collaboration [104], whereas the dashed lines are the results of their A-dependent global fit to nuclear EMC effect. The data and parameterization are both normalized to take into account any hadron attenuation effects.

show data both before and after the events from diffractive ρ production are removed to demonstrate a slightly larger impact on the π^- data. The dashed line represents the A-dependent EMC effect fit from the SLAC collaboration [104] fit. The parameterization is normalized to take into account hadron attenuation effects. Overall, the agreement is quite good, even if our data scatter somewhat and the x-dependence of the cross section ratio Al/D is weak in this region. This confirms that nuclear ratios already behave like a high-energy parton model expectation at relatively low energies and W^2.

The Al/D cross section ratios versus Q^2 are extracted using again our Monte Carlo simulations to "bin-center" the data to a fixed $x = 0.40$. We show the extracted ratios for both π^+ and π^- data at $z = 0.55$ and $x = 0.40$ as a function of Q^2 in Fig. 20. The multiplicity ratio for Al/D is nearly flat with Q^2, comparable to what was also observed for the D/H ratio in Fig.16. Similarly, only a very weak Q^2 dependence for this ratio was observed by the HERMES experiment [100, 105, 106]. The dashed lines represent constant fits to the data, with a best-fit value for π^+ (π^-) of 0.556 ± 0.011 (0.520 ± 0.011).

Recently, there has been discussion on a possible flavor dependence of the EMC effect [107]. This would result in a possible different depletion of up quarks as compared to down quarks. Predictions indicate a somewhat larger depletion for up quarks than for down quarks, or equivalently larger π^+ attenuation than π^- attenuation. We find the opposite, although the uncertainties are large and many complicated nuclear effects may contribute, including effects that do not obey a factorized form. Further study of this requires precision measurement of the z- and x-dependences of these ratios, and their differences [108, 109].

F. The P_t dependence of the cross sections

The extracted cross sections as a function of the pion transverse momentum squared P_t^2 are shown in Fig. 21 and listed in Table XIII.

The solid lines are exponential fits. The acceptance-averaged values of $\cos\phi$ range from -0.3 at low P_t to nearly -1 at high P_t, while the average values of $\cos 2\phi$ range from 0.03 at $P_t \leq 0.1$ to 1 at high P_t.

A recent study [110] analyzed these data in combination with the CLAS data [111], and concluded that in the kinematics similar to the CLAS data, the Hall C data could be relatively well described by a Gaussian model with average transverse momentum width of 0.24 $(\mathrm{GeV/c})^2$. The good description of the $\pi^\pm$ cross sections from different targets was argued to indicate that the assumption of flavor-independent Gaussian width for both the transverse widths of quark and fragmentation functions was reasonable, in the valence-x region for z=0.55.

If taken as standalone data, a careful examination of Fig. 21 shows that the P_t^2-dependences for the four cases are similar, but not identical within statistical uncertainties. For a more quantitative understanding of the possible implications, we study the data in the context of a simple model in which the P_t dependence is described in terms of two Gaussian distributions for each case.

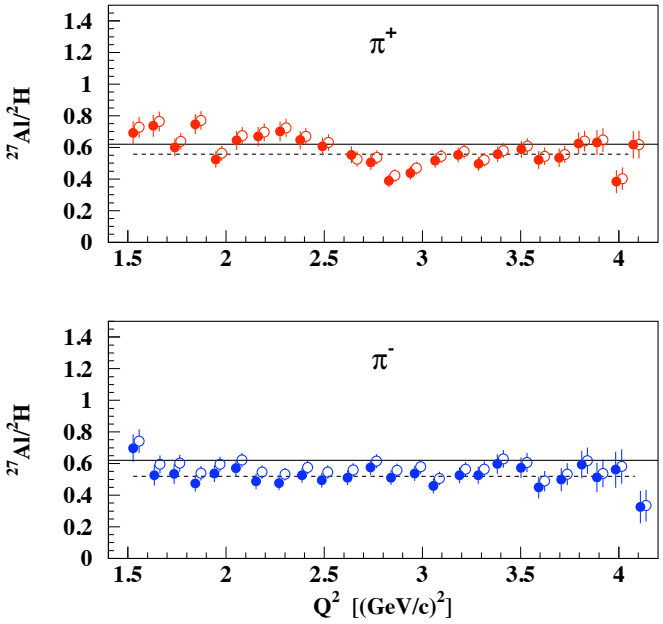

FIG. 20: (Color online) The ratio aluminum over deuteron for π^+ and π^- as a function of Q^2 at $z = 0.55$ and $x = 0.40$. Solid (open) symbols are data after (before) events from diffractive ρ production are subtracted. The solid curves represent a constant value of 0.62, as expected from the gluon radiation calculation at $z = 0.55$. The dashed lines represent constant fits to the data, with value for π^+ (π^-) of 0.556±0.011 (0.520±0.011).

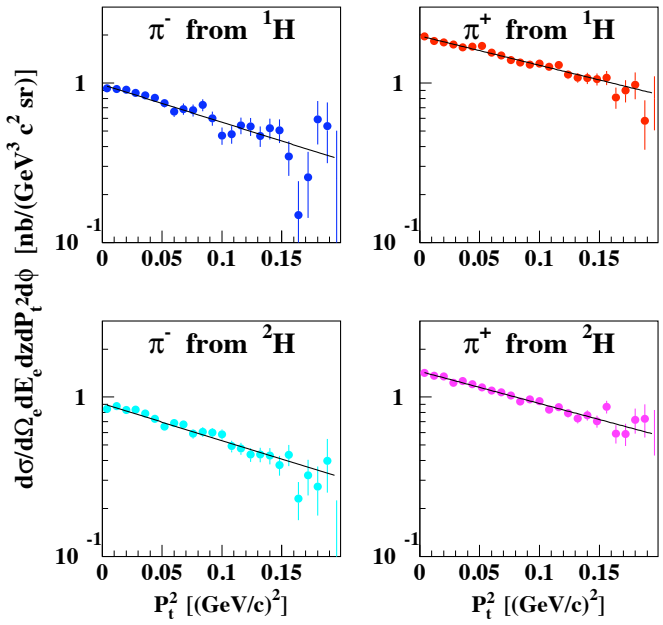

FIG. 21: (Color online) The P_t^2 dependence of differential cross sections per nucleon for $\pi^\pm$ production on hydrogen (H) and deuterium (D) targets at $\langle z\rangle$=0.55 and $\langle x\rangle$=0.32. The solid lines are exponential fits. The error bars are statistical only.

The probability of producing a pion with a transverse momentum P_t relative to the virtual photon ($\vec{q}$) direction is described by a convolution of the quark distribution functions and p_t-dependent fragmentation functions $D^+(z, p_t)$ and $D^-(z, p_t)$, where p_t is the transverse momentum of the pion relative to the quark direction, with the condition $P_t = zk_t + p_t$ assumed.

Following Ref. [57], we assume that the widths of the quark and fragmentation functions are Gaussian and that the convolution of these distributions combines quadratically. The main difference from Ref. [57] is that we allow separate widths for up and down quarks, and separate widths for favored and unfavored fragmentation functions. The widths of the up and down distributions are denoted by μ_u and μ_d, respectively, and the favored (unfavored) fragmentation widths are given by μ_+ (μ_-). Following Cahn [58] and more recent studies [57], we assume that only the fraction z of the quark transverse momentum contributes to the pion transverse momentum. We assume further that sea quarks are negligible (typical global fits show less than 10% contributions at $x = 0.3$). To make the problem tractable, in the ϕ-dependence we take only the leading-order terms in (P_t/Q), which was shown to be a reasonable approximation up to moderate P_t in Ref. [57]. This simple model then gives:

$$\begin{aligned}
\sigma_p^{\pi^+}(P_t) &= C[4c_1(P_t)e^{-b_u^+ P_t^2} + (\tfrac{d}{u})(\tfrac{D^-}{D^+})c_2(P_t)e^{-b_d^- P_t^2}] \\
\sigma_p^{\pi^-}(P_t) &= C[4(\tfrac{D^-}{D^+})c_3(P_t)e^{-b_u^- P_t^2} + (\tfrac{d}{u})c_4(P_t)e^{-b_d^+ P_t^2}] \\
\sigma_n^{\pi^+}(P_t) &= C[4(\tfrac{d}{u})c_4(P_t)e^{-b_d^+ P_t^2} + (\tfrac{D^-}{D^+})c_3(P_t)e^{-b_u^- P_t^2}] \\
\sigma_n^{\pi^-}(P_t) &= C[4(\tfrac{d}{u})(\tfrac{D^-}{D^+})c_2(P_t)e^{-b_d^- P_t^2} + c_1(P_t)e^{-b_u^+ P_t^2}],
\end{aligned} \tag{23}$$

where C is an arbitrary normalization factor, and the inverse of the total widths for each combination of quark flavor and fragmentation function are given by

$$\begin{aligned}
b_u^\pm &= (z^2\mu_u^2 + \mu_\pm^2)^{-1} \\
b_d^\pm &= (z^2\mu_d^2 + \mu_\pm^2)^{-1}
\end{aligned} \tag{24}$$

and we assume $\sigma_d = (\sigma_p + \sigma_n)/2$. The ϕ-dependence is taken into account through the terms:

$$\begin{aligned}
c_1(P_t) &= 1 + c_0(P_t, \langle\cos(\phi)\rangle)\mu_u^2 b_u^+ \\
c_2(P_t) &= 1 + c_0(P_t, \langle\cos(\phi)\rangle)\mu_d^2 b_d^- \\
c_3(P_t) &= 1 + c_0(P_t, \langle\cos(\phi)\rangle)\mu_u^2 b_u^- \\
c_4(P_t) &= 1 + c_0(P_t, \langle\cos(\phi)\rangle)\mu_d^2 b_d^+ \\
c_0(P_t, \langle\cos(\phi)\rangle) &= \tfrac{4z(2-y)\sqrt{1-y}}{\sqrt{Q^2}[1+(1-y)^2]}\sqrt{P_t^2}\langle\cos(\phi)\rangle.
\end{aligned} \tag{25}$$

We fit the P_t-dependence of the four cross sections of Eq. 23 for the four widths (μ_u, μ_d, μ_+, and μ_-), C, and the ratios D^-/D^+ and d/u, where the fragmentation ratio is understood to represent the data-averaged value at $z = 0.55$, and the quark distribution ratio is understood to represent the average value at $x = 0.3$. The fit describes the data reasonably well ($\chi^2 = 68$ for 73 degrees of freedom), and finds the ratio $d/u = 0.39\pm0.03$, in good agreement with the LO GRV98 fit [32] for valence quarks (about 0.40). The fit also gives a reasonable value for the

ratio $D^-/D^+ = 0.43\pm0.01$ (a fit to HERMES results [91], $D^-/D^+ = 1/(1+z)^2$, predicts 0.42 at $z = 0.55$). Both d/u and D^-/D^+ are largely uncorrelated with the other fit parameters and their values are largely determined by the magnitude of the cross sections. To estimate the effect of experimental systematic uncertainties on our fit results, we repeated the fits with: no diffractive ρ subtraction; 30% smaller exclusive radiative tail subtraction; relative target thickness changed by 1%; and difference in π^+ and π^- absorptions changed by 1%. The last three changes had a negligible effect compared to statistical errors. The first change mainly affected μ_-^2, shifting it to a more positive value by almost the size of the statistical error, as shown in Fig. 22. We found no significant change to the fit parameters upon adding to μ_u^2 and μ_d^2 an average nucleon transverse momentum squared of 0.001 $(\mathrm{GeV}/c)^2$ (evaluated using the Paris wave function [112]) for the deuteron model.

Since the data are at fixed z, the main terms that distinguish large fragmentation widths from large quark widths are the ϕ-dependent c_i terms. While there is a significant inverse correlation between the two most important quark and fragmentation widths, (μ_u and μ_+, respectively), the fit indicates a preference for μ_u to be smaller than μ_+ as shown in Fig. 22a. The fit also indicates a preference for μ_d to be smaller than μ_- as shown in Fig. 22b. So in both cases, fragmentation widths appear to somewhat dominate over quark widths, within our simple model.

The fit parameters indicate a non-zero k_t width squared for u quarks ($\mu_u^2 = 0.07 \pm 0.03$ $(\mathrm{GeV}/c)^2$), but a d-quark width squared that is consistent with zero ($\mu_d^2 = -0.01 \pm 0.05$ $(\mathrm{GeV}/c)^2$), as illustrated in Fig. 22c. We do note that intrinsic transverse momentum width for u and d quarks presented here are far different from the earlier published [94]. The previous analysis results used a limited and not required cut in the reconstructed vertex coordinate reducing statistics, and also has improper corrections for contributions of pions from both the decay of diffractive ρ production and the exclusive radiative tail. Still, the difference in the two results calls for a future careful measurement over a large of kinematics (Q^2, P_t and $cos(\phi)$).

The results are consistent with a di-quark model [113] in which the d quarks are only found in an axial di-quark, while the u quarks are predominantly found in a scalar di-quark. We plotted the results with equal axial and scalar di-quarks masses (M_a and M_s) of 0.6 GeV; picking $M_a < M_s$ results in $\mu_d^2 < \mu_u^2$, and visa verse, with the average remaining near 0.06 $(\mathrm{GeV}/c)^2$.

Using the fit parameters, we find the magnitude of the $\cos(\phi)$ term A at $P_t = 0.4$ GeV/c to be about -0.15 ± 0.05 for all four cases. These results are similar in sign and magnitude to those found in the HERMES experiment [114].

We find that the fragmentation widths μ_+ and μ_- are correlated, as illustrated in Fig. 22d, although the allowed range is not large, and the central values ($\mu_+^2 =$ 0.18 ± 0.02 $(\mathrm{GeV}/c)^2$ and $\mu_-^2 = 0.14 \pm 0.02$ $(\mathrm{GeV}/c)^2$) are in reasonable agreement with each other and with the flavor-averaged value of 0.20 $(\mathrm{GeV}/c)^2$ found in Ref. [57]. While there is a slight tendency for the favored width to be larger than the unfavored one, a reasonable fit can be obtained setting the widths equal to each other ($\chi^2 = 71$ for 74 d.f., $\mu_+^2 = \mu_-^2 = 0.17\pm0.03$ $(\mathrm{GeV}/c)^2$). Taking into account the systematic uncertainties, the favored and unfavored widths are consistent with each other.

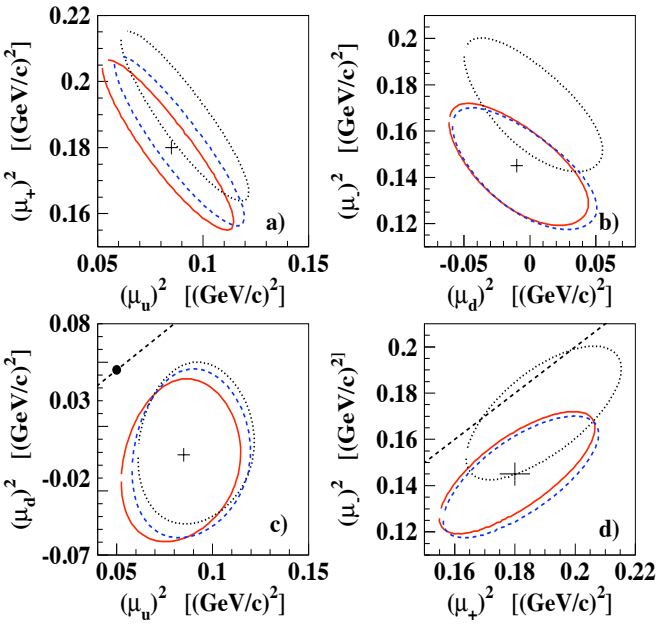

FIG. 22: (Color online) Fit parameters (crosses) and one-standard-deviation contours (continuous ellipses) from the seven-parameter fit to the data shown in Fig. 21: a) u quark width squared μ_u^2 versus favored fragmentation width squared μ_+^2; b) μ_d^2 versus μ_-^2; c) μ_u^2 versus μ_d^2; d) μ_-^2 vs μ_+^2. The dashed and dotted contours are for the case of no diffractive ρ subtraction and a 30% reduction in the size of the exclusive radiative tail subtraction, respectively. The large dot near the middle of panel c is from a di-quark model [113]. The dashed straight lines in panels c and d indicate $\mu_u^2 = \mu_d^2$ and $\mu_-^2 = \mu_+^2$, respectively.

G. The P_t dependence of the ratios

π^+/π^- ratios versus P_t^2: The ratios of charged pions for proton, deuteron and aluminum targets as a function of P_t^2 at $z = 0.55$ and $x = 0.32$ are shown in Fig. 23. Solid (open) symbols are our data after (before) events from ρ decay are subtracted. The solid lines represent the expectations from the simple quark-parton model.

The average values of the pion ratios for deuteron and aluminum are smaller than that for the proton, but they are nearly flat with P_t^2 for all three targets.

D/H ratios versus P_t^2: The deuteron over proton ratios for π^+ (top panel) and π^- (bottom) as a function of

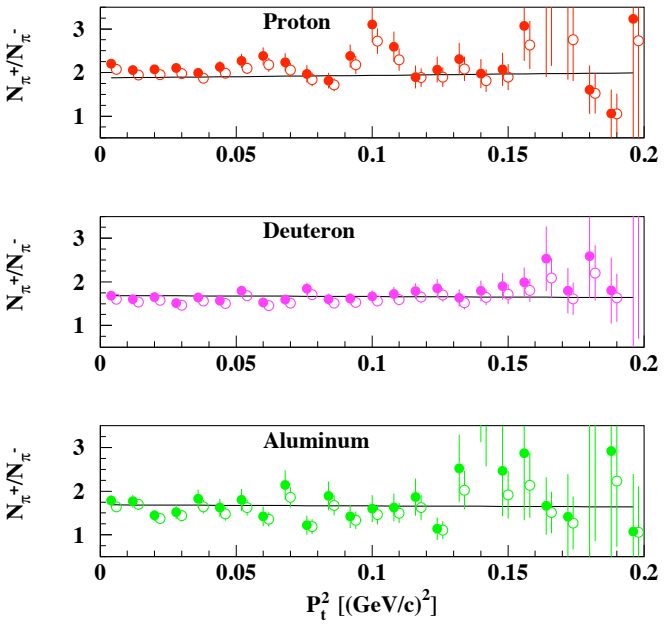

FIG. 23: (Color online) The ratio π^+/π^- for proton, deuteron and aluminum as a function of P_t^2 at $z = 0.55$ and $x = 0.32$. Solid (open) symbols are our data after (before) events from diffractive ρ decay are subtracted. The solid lines are simple quark-parton model expectations.

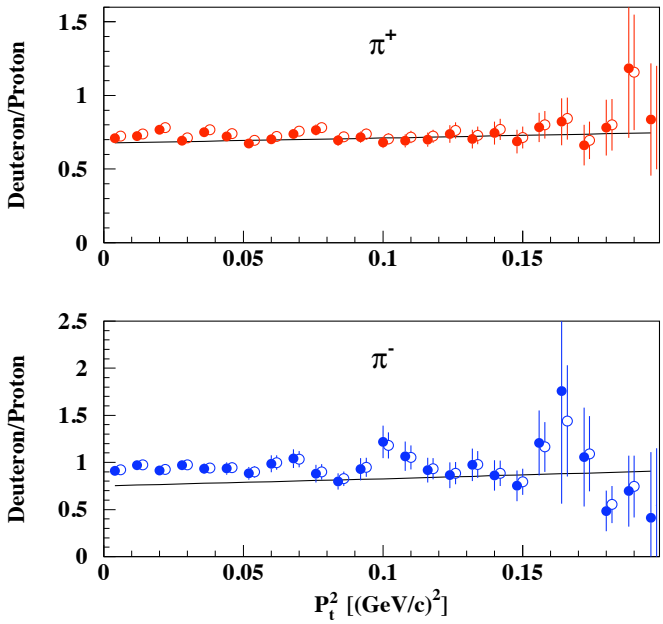

FIG. 24: (Color online) The ratio deuteron over proton for π^+ (top panel) and π^- (bottom) as a function of P_t^2 at $z = 0.55$ and $x = 0.32$. Solid (open) symbols are our data after (before) events from diffractive ρ decay are subtracted. The solid lines are our simple quark-parton model expectations.

P_t^2 at $z = 0.55$ and $x = 0.32$ are shown in Fig. 24. Solid (open) symbols are our data after (before) events from ρ decay are subtracted. The solid lines shown correspond as before to the simple quark-parton model calculation. As can be seen, the D/H ratios for π^+ are in good agreement with the quark-parton model prediction. For π^- the experimental data on average are ∼10-15% higher relative to the model expectation.

P_t^2 dependence of the d_v/u_v ratios: For fixed x = 0.32 (Q^2 = 2.30 (GeV/c)^2) and z = 0.55, we show in Fig. 25 the extracted ratios of the down to up valence quark distributions d_v/u_v as a function of P_t^2. The extracted ratios shown before, as function of x and z in Fig. 17, were from the lowest P_t^2 bin only. As before, the extracted ratios are on average below the quark-parton model expectations, here based upon the GRV parton distributions but also consistent with the earlier comparisons with CTEQ parton distributions. Given the statistical precision of the E00-108 data, it can not be ruled out that the d_v/u_v valence quark distribution ratio may have a dependence on P_t (or intrinsic quark momentum k_t). Such a dependence is in principle possible within a transverse-momentum dependent framework [94]. It has been calculated to be small for up and down spin-averaged parton distributions in Lattice QCD, with far larger dependences found in spin-dependent parton distributions [115].

P_t^2 dependence of the Al/D ratios: In Fig. 26 the ratio aluminum over deuteron for π^+ and π^- as a function of P_t^2 at $x = 0.32$ and $z = 0.55$ is shown. Solid

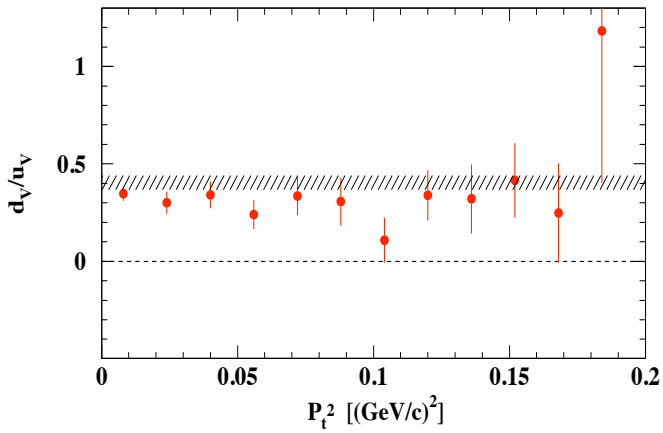

FIG. 25: (Color online) The extracted ratio d_v/u_v as a function of P_t^2 at x=0.32 and z=0.55. The solid circles are the E00-108 data after events from diffractive ρ decay are subtracted. The dashed band is a quark-parton model expectation using CTEQ parton distribution function parameterizations [90].

(open) symbols are data after (before) events from coherent ρ production are subtracted. The data show that the Al/D ratio is reduced at high z, as was observed by HERMES group [105]. Our data show slight differences in attenuation of π^+ and π^-. The reduction seems to be stronger for π^+.

In our kinematic range the multiplicity ratio for Al/D

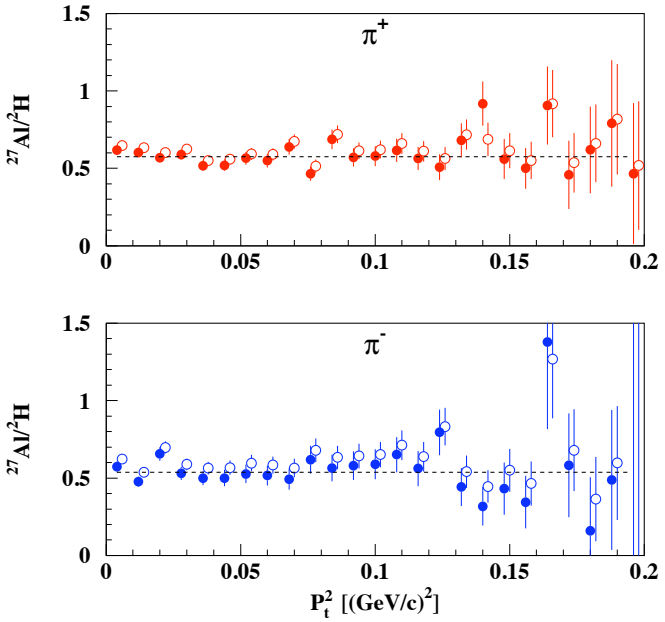

FIG. 26: (Color online) The cross section ratio aluminum over deuteron for π^+ (top) and π^- (bottom) as a function of P_t^2 at $x = 0.32$ and $z = 0.55$. Solid (open) symbols are data after (before) events from diffractive ρ production are subtracted. The dashed lines are constant fits to the data.

as a function of P_t^2 is nearly flat. The dashed lines in Fig. 26 represent constant fits to the data, with a best-fit value for π^+ and π^- of 0.575±0.010 and 0.538±0.014, and a χ^2/ndf of 1.23 and 1.16, respectively. Similar flat behavior for the region $P_t^2 \leq 0.2$ (GeV/c)^2 was observed by HERMES group for variety of nuclei.

For future use, we have presented in this manuscript the various ratios versus z, x and P_t^2 in tabular format in Tables XIV-XIX.

VIII. SUMMARY AND CONCLUSIONS

In summary, we have measured semi-inclusive electroproduction of charged pions ($\pi^{\pm}$) from both proton and deuteron targets, using a 5.479 GeV energy electron beam in Hall C at Jefferson Lab. We have observed, for the first time, the quark-hadron duality phenomenon in pion electroproduction reactions. This has important consequences for a viable access to a quark-parton model description in semi-inclusive deep inelastic scattering experiments at relatively low energies. Several ratios constructed from the data exhibit, provided that $W^2 > 4.0$ GeV^2 and $z < 0.7$ (or beyond the Δ-resonance region in missing mass), the features of factorization in a sequential electron-quark scattering and a quark-pion fragmentation process. We find the azimuthal dependence of the data to be small, as compared to the typically larger azimuthal dependences found in exclusive pion electroproduction data, but consistent with data from other groups and theoretical expectations [57, 58] based on a semi-inclusive deep inelastic scattering approach.

Examination of the P_t dependence of the cross section shows a possible flavor dependence of the transverse-momentum dependence of the quark distribution and/or fragmentation functions. In the context of a simple model with only valence quarks and only two fragmentation functions, we find the transverse momentum k_t width of u quarks to be larger than that for d quarks, for which the width is consistent with zero within the statistical uncertainties. We find that the transverse momentum p_t widths of the favored and unfavored fragmentation functions are similar to each other, and both larger than the two quark widths. This is consistent with theoretical expectations based on fits to the world data. We have shown the sensitivity of our results to be small to possible corrections due to both radiative events from exclusive pion production channels and pions originating from diffractive ρ scattering (and decay). In many cases, the corrections are negligible, although they can become large at large values of z. We believe our work will provide a fruitful basis for future studies of the quark-parton model and more sophisticated model calculations at relatively low energies.

ACKNOWLEDGMENTS

The authors wish to thank H. Avakian, A. Afanasev, A Bruell, C.E. Carlson, W. Melnitchouk and M. Schlegel for discussions, and for many useful suggestions. This work is supported in part by research grants from the U.S. Department of Energy DE-FG02-99ER-41065 (Florida International University), DE-AC02-06CH11357 (Argonne National Laboratory), DE-FG02-04ER41330 (Mississippi State University), and the U.S. National Science Foundation #0072466 and 0347438 (North Carolina A&T State University), and #0400332 and 0653508 (Hampton University). We acknowledge support from the Natural Sciences and Engineering Research Council of Canada (University of Regina), and the South African National Research Foundation (University of Johannesburg). The Southeastern Universities Research Association operates the Thomas Jefferson National Accelerator Facility under the U.S. Department of Energy contract DEAC05-84ER40150.

TABLE XIII: Experimental differential cross sections per nucleus (in nb/GeV$^3/c^2/sr$) versus P_t^2 (in GeV$^2/c^2$) for π^+ and π^- production on Hydrogen and Deuterium targets. Left (right) part of the table represents the values before (after) events from diffractive ρ decay have been subtracted. Error bars are statistical only.

P_t^2	$\sigma_H^+ \pm d\sigma$	$\sigma_H^- \pm d\sigma$	$\sigma_D^+ \pm d\sigma$	$\sigma_D^- \pm d\sigma$	$\sigma_H^+ \pm d\sigma$	$\sigma_H^- \pm d\sigma$	$\sigma_D^+ \pm d\sigma$	$\sigma_D^- \pm d\sigma$
0.004	2.068±0.029	1.039±0.022	3.052±0.040	1.912±0.034	1.959±0.029	0.927±0.022	2.831±0.039	1.688±0.034
0.012	1.943±0.031	1.033±0.026	2.951±0.041	1.982±0.040	1.832±0.031	0.916±0.026	2.727±0.041	1.754±0.039
0.020	1.910±0.035	1.023±0.031	2.925±0.046	1.884±0.048	1.798±0.035	0.908±0.031	2.700±0.046	1.655±0.047
0.028	1.857±0.040	0.983±0.038	2.682±0.051	1.899±0.058	1.745±0.039	0.866±0.037	2.457±0.051	1.668±0.057
0.036	1.789±0.043	0.954±0.042	2.754±0.059	1.811±0.064	1.674±0.042	0.838±0.041	2.521±0.058	1.579±0.063
0.044	1.810±0.046	0.925±0.045	2.630±0.063	1.685±0.065	1.695±0.045	0.807±0.044	2.405±0.062	1.458±0.065
0.052	1.820±0.047	0.862±0.046	2.523±0.066	1.531±0.068	1.711±0.047	0.747±0.046	2.303±0.066	1.305±0.067
0.060	1.656±0.047	0.775±0.049	2.415±0.069	1.597±0.073	1.549±0.046	0.662±0.048	2.197±0.068	1.377±0.072
0.068	1.605±0.049	0.806±0.056	2.367±0.073	1.571±0.079	1.491±0.049	0.687±0.056	2.145±0.072	1.347±0.078
0.076	1.507±0.049	0.788±0.060	2.263±0.074	1.397±0.080	1.397±0.049	0.676±0.059	2.050±0.073	1.178±0.079
0.084	1.455±0.051	0.843±0.064	2.094±0.077	1.433±0.084	1.344±0.051	0.730±0.063	1.874±0.076	1.210±0.084
0.092	1.414±0.053	0.710±0.061	2.144±0.081	1.410±0.086	1.305±0.053	0.602±0.061	1.931±0.080	1.197±0.085
0.100	1.430±0.056	0.572±0.058	2.101±0.085	1.380±0.087	1.323±0.056	0.468±0.058	1.890±0.084	1.171±0.086
0.108	1.383±0.061	0.587±0.060	1.886±0.084	1.196±0.082	1.268±0.060	0.477±0.060	1.671±0.083	0.985±0.081
0.116	1.412±0.067	0.648±0.064	1.935±0.090	1.152±0.084	1.300±0.066	0.542±0.064	1.730±0.089	0.951±0.083
0.124	1.237±0.069	0.638±0.069	1.787±0.095	1.068±0.086	1.129±0.068	0.535±0.069	1.587±0.093	0.872±0.085
0.132	1.182±0.074	0.565±0.069	1.663±0.102	1.062±0.091	1.081±0.074	0.466±0.068	1.470±0.101	0.873±0.090
0.140	1.180±0.088	0.625±0.079	1.735±0.116	1.058±0.100	1.074±0.087	0.521±0.078	1.537±0.115	0.858±0.099
0.148	1.157±0.093	0.605±0.086	1.601±0.125	0.947±0.108	1.057±0.092	0.506±0.085	1.407±0.123	0.751±0.107
0.156	1.177±0.109	0.440±0.086	1.933±0.164	1.065±0.135	1.081±0.108	0.347±0.085	1.737±0.162	0.870±0.134
0.164	0.922±0.125	0.255±0.094	1.368±0.160	0.650±0.124	0.814±0.124	0.149±0.093	1.178±0.157	0.461±0.123
0.172	1.001±0.143	0.357±0.114	1.370±0.189	0.840±0.164	0.899±0.142	0.257±0.114	1.173±0.186	0.646±0.163
0.180	1.073±0.189	0.686±0.181	1.614±0.259	0.725±0.188	0.978±0.187	0.593±0.180	1.436±0.255	0.548±0.186
0.188	0.684±0.201	0.637±0.223	1.677±0.350	1.013±0.297	0.580±0.199	0.536±0.222	1.458±0.345	0.797±0.293
0.196	0.878±0.302	0.323±0.252	1.394±0.404	0.324±0.260	0.805±0.299	0.250±0.252	1.257±0.399	0.189±0.259

TABLE XIV: The $R = \pi^+/\pi^-$ ratios versus Z for H, D and Al targets. Left (right) part of the table represents the ratios before (after) events from diffractive ρ decay have been subtracted. Error bars are statistical only.

z	R_H±dR	R_D±dR	R_{Al}±dR	R_H±dR	R_D±dR	R_{Al}±dR
0.317	1.773±0.311	1.317±0.167	1.330±0.335	1.828±0.340	1.337±0.179	1.358±0.368
0.352	1.710±0.100	1.384±0.065	1.356±0.141	1.756±0.110	1.415±0.072	1.401±0.162
0.387	1.953±0.091	1.508±0.053	1.343±0.117	2.038±0.102	1.553±0.059	1.389±0.136
0.422	1.832±0.076	1.396±0.045	1.483±0.136	1.898±0.084	1.429±0.050	1.556±0.161
0.457	1.832±0.071	1.421±0.045	1.554±0.141	1.898±0.079	1.456±0.049	1.638±0.169
0.493	1.809±0.068	1.455±0.046	1.437±0.124	1.898±0.077	1.501±0.052	1.517±0.153
0.527	1.974±0.072	1.499±0.047	1.672±0.145	2.098±0.084	1.565±0.054	1.848±0.195
0.562	2.061±0.071	1.573±0.047	1.622±0.134	2.194±0.083	1.649±0.054	1.778±0.178
0.597	2.159±0.066	1.519±0.043	1.608±0.123	2.327±0.079	1.597±0.050	1.764±0.166
0.632	1.997±0.061	1.584±0.045	1.445±0.109	2.178±0.075	1.681±0.054	1.577±0.149
0.668	1.814±0.051	1.542±0.040	1.773±0.128	1.970±0.064	1.657±0.051	2.101±0.203
0.702	1.787±0.052	1.501±0.039	1.555±0.116	1.947±0.066	1.608±0.049	1.792±0.182
0.738	1.637±0.047	1.613±0.040	1.742±0.138	1.760±0.060	1.755±0.051	2.111±0.243
0.772	1.479±0.041	1.713±0.039	1.506±0.108	1.580±0.053	1.916±0.053	1.784±0.185
0.808	1.269±0.033	1.806±0.038	1.776±0.129	1.323±0.040	2.018±0.052	2.061±0.228
0.842	1.267±0.029	1.929±0.039	1.718±0.140	1.306±0.034	2.133±0.050	1.936±0.256
0.877	1.499±0.041	1.912±0.046	1.735±0.173	1.574±0.049	2.109±0.060	2.184±0.325
0.913	2.257±0.227	1.111±0.100	0.683±0.268	2.746±0.359	1.140±0.127	0.528±0.382

TABLE XV: The $R = \pi^+/\pi^-$ ratios versus X for H, D and Al targets. Left (right) part of the table represents the ratios before (after) events from diffractive ρ decay have been subtracted. Error bars are statistical only.

x	$R_H \pm$dR	$R_D \pm$dR	$R_{Al} \pm$dR	$R_H \pm$dR	$R_D \pm$dR	$R_{Al} \pm$dR
0.208	1.773±0.139	1.349±0.086	1.338±0.157	1.894±0.172	1.410±0.103	1.426±0.204
0.224	1.371±0.089	1.358±0.073	1.607±0.186	1.427±0.105	1.418±0.087	1.742±0.260
0.240	1.823±0.099	1.509±0.071	1.474±0.158	1.946±0.119	1.595±0.085	1.612±0.218
0.256	1.765±0.090	1.392±0.059	1.692±0.174	1.867±0.106	1.447±0.068	1.886±0.242
0.272	1.899±0.093	1.526±0.061	1.344±0.137	2.021±0.110	1.600±0.071	1.413±0.178
0.288	1.948±0.091	1.494±0.059	1.507±0.141	2.064±0.106	1.559±0.068	1.594±0.178
0.304	2.025±0.096	1.527±0.058	1.524±0.153	2.142±0.111	1.593±0.067	1.596±0.195
0.320	1.958±0.091	1.446±0.055	1.993±0.193	2.063±0.104	1.496±0.062	2.213±0.258
0.336	2.073±0.100	1.481±0.055	1.763±0.168	2.197±0.116	1.538±0.063	1.914±0.215
0.352	1.991±0.095	1.536±0.058	1.711±0.175	2.091±0.108	1.596±0.065	1.843±0.223
0.368	2.083±0.097	1.632±0.061	1.641±0.168	2.179±0.109	1.702±0.069	1.784±0.212
0.384	2.344±0.110	1.516±0.056	1.318±0.132	2.481±0.126	1.560±0.063	1.372±0.158
0.400	1.966±0.096	1.725±0.063	1.249±0.144	2.038±0.107	1.801±0.071	1.290±0.176
0.416	2.292±0.115	1.618±0.061	1.262±0.139	2.409±0.130	1.680±0.068	1.294±0.165
0.432	2.198±0.111	1.553±0.059	1.746±0.191	2.306±0.124	1.604±0.066	1.887±0.240
0.448	2.101±0.117	1.576±0.061	1.497±0.162	2.178±0.131	1.627±0.068	1.570±0.192
0.464	2.129±0.120	1.577±0.065	1.292±0.154	2.220±0.134	1.626±0.072	1.326±0.179
0.480	2.385±0.148	1.618±0.072	1.521±0.180	2.505±0.166	1.668±0.080	1.595±0.211
0.496	2.615±0.173	1.545±0.073	1.431±0.180	2.755±0.195	1.587±0.080	1.487±0.208
0.512	2.680±0.189	1.554±0.079	1.671±0.265	2.803±0.211	1.598±0.087	1.782±0.322
0.528	2.131±0.162	1.571±0.089	1.554±0.242	2.205±0.177	1.613±0.096	1.630±0.284
0.544	2.061±0.189	1.535±0.095	1.444±0.233	2.129±0.206	1.566±0.102	1.483±0.259
0.560	2.122±0.210	1.454±0.099	1.352±0.247	2.191±0.228	1.479±0.106	1.377±0.270
0.576	2.112±0.217	1.584±0.122	1.061±0.272	2.161±0.230	1.613±0.130	1.059±0.298
0.592	1.946±0.238	1.867±0.169	2.257±0.642	1.953±0.240	1.879±0.171	2.242±0.643

[1] E. D. Bloom and F. J. Gilman, Phys. Rev. Lett. **25**,

[2] P. D. B. Collins, An Introduction to Regge Theory

TABLE XVI: The $R = \pi^+/\pi^-$ ratios versus P_t^2 (in GeV$^2/c^2$) for H, D and Al targets. Left (right) part of the table represents the ratios before (after) events from diffractive ρ decay have been subtracted. Error bars are statistical only.

P_t^2	R_H±dR	R_D±dR	R_{Al}±dR	R_H±dR	R_D±dR	R_{Al}±dR
0.004	2.072±0.059	1.601±0.039	1.638±0.103	2.201±0.069	1.679±0.045	1.784±0.133
0.012	1.940±0.065	1.535±0.041	1.695±0.119	2.058±0.075	1.603±0.047	1.770±0.146
0.020	1.951±0.077	1.575±0.050	1.372±0.101	2.071±0.090	1.653±0.059	1.444±0.126
0.028	1.978±0.093	1.464±0.054	1.436±0.125	2.109±0.110	1.516±0.063	1.523±0.162
0.036	1.873±0.099	1.564±0.064	1.642±0.154	1.991±0.117	1.645±0.076	1.826±0.210
0.044	1.982±0.113	1.508±0.068	1.479±0.154	2.126±0.136	1.573±0.080	1.621±0.209
0.052	2.099±0.131	1.682±0.085	1.621±0.181	2.266±0.160	1.793±0.104	1.801±0.254
0.060	2.176±0.157	1.460±0.078	1.361±0.170	2.378±0.196	1.529±0.093	1.425±0.226
0.068	2.056±0.164	1.512±0.089	1.859±0.232	2.239±0.205	1.595±0.108	2.141±0.337
0.076	1.842±0.161	1.710±0.111	1.186±0.168	1.970±0.198	1.844±0.140	1.220±0.217
0.084	1.714±0.146	1.512±0.105	1.677±0.232	1.815±0.175	1.605±0.129	1.891±0.331
0.092	2.176±0.207	1.528±0.108	1.333±0.199	2.379±0.262	1.617±0.133	1.424±0.266
0.100	2.722±0.294	1.563±0.115	1.459±0.223	3.098±0.402	1.663±0.142	1.599±0.307
0.108	2.294±0.256	1.595±0.127	1.497±0.232	2.591±0.349	1.723±0.164	1.628±0.320
0.116	1.884±0.215	1.649±0.138	1.627±0.283	1.896±0.263	1.786±0.178	1.864±0.425
0.124	1.897±0.228	1.701±0.157	1.108±0.200	2.069±0.292	1.857±0.206	1.138±0.259
0.132	2.083±0.279	1.525±0.154	2.023±0.441	2.312±0.369	1.631±0.197	2.527±0.769
0.140	1.813±0.258	1.645±0.182	3.418±0.843	1.976±0.332	1.795±0.239	5.186±2.065
0.148	1.896±0.298	1.716±0.225	1.913±0.543	2.073±0.384	1.904±0.307	2.467±1.041
0.156	2.631±0.553	1.808±0.260	2.135±0.746	3.071±0.803	1.989±0.343	2.871±1.527
0.164	3.509±1.355	2.088±0.451	1.511±0.480	5.313±3.421	2.533±0.741	1.663±0.660
0.172	2.754±0.945	1.612±0.368	1.271±0.607	3.439±1.600	1.797±0.520	1.412±0.979
0.180	1.525±0.462	2.205±0.639	4.001±3.144	1.607±0.556	2.593±0.962	10.05±21.82
0.188	1.049±0.463	1.631±0.551	2.233±1.506	1.058±0.555	1.802±0.756	2.917±2.849
0.196	2.727±2.279	4.250±3.553	1.060±1.050	3.235±3.431	6.571±9.187	1.075±1.323

TABLE XVII: The deuteron over proton ($R_{D/H}$= D/H) and aluminum over deuteron ($R_{Al/D}$=Al/D) ratios for π^+ and π^- versus z. Left (right) part of the table represents the ratios before (after) events from diffractive ρ decay have been subtracted. Error bars are statistical only.

z	$R^+_{D/H}$±dR	$R^-_{D/H}$±dR	$R^+_{Al/D}$±dR	$R^-_{Al/D}$±dR	$R^+_{D/H}$±dR	$R^-_{D/H}$±dR	$R^+_{Al/D}$±dR	$R^-_{Al/D}$±dR
0.317	0.814±0.109	1.115±0.192	0.770±0.146	0.763±0.159	0.806±0.112	1.123±0.207	0.759±0.153	0.747±0.168
0.352	0.733±0.034	0.927±0.055	0.689±0.052	0.691±0.060	0.721±0.035	0.920±0.059	0.670±0.055	0.663±0.065
0.387	0.773±0.025	1.024±0.050	0.622±0.038	0.688±0.049	0.763±0.026	1.025±0.054	0.600±0.040	0.659±0.053
0.422	0.747±0.023	0.985±0.043	0.636±0.039	0.597±0.045	0.736±0.024	0.981±0.046	0.614±0.041	0.563±0.049
0.457	0.748±0.023	0.995±0.040	0.631±0.039	0.579±0.043	0.737±0.023	0.995±0.043	0.610±0.041	0.543±0.046
0.493	0.758±0.024	0.973±0.037	0.602±0.038	0.618±0.041	0.744±0.025	0.970±0.041	0.573±0.041	0.575±0.046
0.527	0.702±0.023	0.980±0.034	0.635±0.038	0.562±0.039	0.685±0.024	0.977±0.039	0.605±0.041	0.504±0.044
0.562	0.742±0.024	1.004±0.033	0.601±0.035	0.576±0.038	0.727±0.025	1.003±0.038	0.569±0.037	0.520±0.043
0.597	0.702±0.020	1.039±0.032	0.606±0.033	0.577±0.035	0.683±0.021	1.041±0.037	0.570±0.036	0.517±0.040
0.632	0.778±0.022	1.052±0.033	0.579±0.032	0.635±0.037	0.760±0.024	1.060±0.039	0.536±0.035	0.572±0.043
0.668	0.795±0.021	1.016±0.029	0.670±0.033	0.582±0.034	0.774±0.023	1.017±0.036	0.628±0.037	0.494±0.041
0.702	0.802±0.021	1.063±0.031	0.607±0.033	0.584±0.034	0.781±0.023	1.077±0.039	0.553±0.037	0.493±0.040
0.738	0.882±0.023	1.025±0.030	0.580±0.031	0.526±0.033	0.868±0.025	1.030±0.038	0.524±0.035	0.416±0.040
0.772	0.996±0.024	1.004±0.029	0.540±0.027	0.612±0.034	0.996±0.028	1.002±0.037	0.472±0.031	0.507±0.043
0.808	1.115±0.026	0.898±0.024	0.543±0.025	0.542±0.032	1.130±0.030	0.875±0.029	0.483±0.028	0.428±0.039
0.842	1.044±0.022	0.802±0.020	0.430±0.021	0.457±0.030	1.048±0.024	0.768±0.023	0.371±0.023	0.339±0.036
0.877	0.933±0.023	0.973±0.032	0.406±0.026	0.448±0.037	0.927±0.025	0.967±0.039	0.345±0.028	0.329±0.044
0.913	0.674±0.067	0.000±0.000	0.382±0.137	0.622±0.117	0.627±0.075	0.000±0.000	0.243±0.165	0.525±0.146
0.947	0.693±0.049	0.049±0.012	1.971±0.119	5.758±1.535	0.693±0.049	0.049±0.012	1.971±0.119	5.758±1.535
0.983	0.330±0.025	0.211±0.019	1.758±0.130	1.748±0.214	0.330±0.025	0.211±0.019	1.758±0.130	1.748±0.214

and High Energy Physics, Cambridge University Press, Cambridge, 1977.

[3] A. Donnachie, G. Dosch, P. Landshoff and O. Nachtman, Pameron Physics and QCD, Cambridge University Press, Cambridge, 2002.

[4] A. De Rújula, H. Georgi, and H. D. Politzer, Phys. Lett. **B64**, 428 (1977); Ann. Phys. **103**, 315 (1977).

[5] G. Domokos, S. Koveni-Domokos, E. Schonberg, Phys. Rev. D **3**, 1184 (1971); D **3**, 1191 (1971); D **4**, 2115 (1971).

TABLE XVIII: The deuteron over proton ($R_{D/H}$= D/H) and aluminum over deuteron ($R_{Al/D}$=Al/D) ratios for π^+ and π^- versus x. Left (right) part of the table represents the ratios before (after) events from diffractive ρ decay have been subtracted. Error bars are statistical only.

x	$R^+_{D/H}\pm$dR	$R^-_{D/H}\pm$dR	$R^+_{Al/D}\pm$dR	$R^-_{Al/D}\pm$dR	$R^+_{D/H}\pm$dR	$R^-_{D/H}\pm$dR	$R^+_{Al/D}\pm$dR	$R^-_{Al/D}\pm$dR
0.208	0.770±0.052	1.102±0.085	0.727±0.066	0.742±0.074	0.748±0.056	1.119±0.103	0.693±0.074	0.698±0.086
0.224	0.873±0.057	0.963±0.057	0.765±0.063	0.595±0.058	0.859±0.062	0.956±0.066	0.737±0.069	0.527±0.067
0.240	0.746±0.040	0.962±0.051	0.639±0.053	0.603±0.054	0.727±0.043	0.955±0.059	0.600±0.057	0.536±0.063
0.256	0.768±0.041	1.023±0.048	0.771±0.058	0.539±0.046	0.749±0.044	1.026±0.055	0.747±0.064	0.474±0.052
0.272	0.744±0.037	0.993±0.046	0.564±0.048	0.595±0.047	0.726±0.039	0.991±0.052	0.524±0.052	0.537±0.053
0.288	0.685±0.034	0.958±0.043	0.673±0.054	0.622±0.046	0.666±0.036	0.947±0.048	0.644±0.059	0.570±0.052
0.304	0.706±0.035	0.962±0.042	0.696±0.057	0.547±0.043	0.689±0.037	0.953±0.047	0.669±0.062	0.487±0.048
0.320	0.719±0.036	0.983±0.040	0.724±0.059	0.533±0.041	0.703±0.038	0.981±0.045	0.701±0.064	0.477±0.046
0.336	0.734±0.035	1.065±0.046	0.670±0.053	0.575±0.042	0.719±0.037	1.072±0.052	0.646±0.057	0.525±0.047
0.352	0.730±0.036	0.947±0.040	0.632±0.052	0.546±0.042	0.715±0.037	0.939±0.044	0.606±0.056	0.494±0.047
0.368	0.687±0.031	0.908±0.038	0.526±0.048	0.560±0.042	0.673±0.032	0.897±0.042	0.553±0.053	0.510±0.047
0.384	0.615±0.027	1.018±0.044	0.536±0.045	0.615±0.043	0.600±0.027	1.020±0.049	0.506±0.048	0.575±0.047
0.400	0.757±0.033	0.926±0.040	0.422±0.039	0.558±0.042	0.746±0.034	0.917±0.044	0.388±0.041	0.511±0.046
0.416	0.655±0.028	0.987±0.046	0.470±0.040	0.579±0.044	0.641±0.029	0.982±0.050	0.439±0.042	0.537±0.048
0.432	0.684±0.029	0.989±0.046	0.544±0.042	0.506±0.043	0.672±0.030	0.988±0.050	0.517±0.045	0.459±0.047
0.448	0.725±0.032	1.008±0.051	0.576±0.045	0.564±0.046	0.715±0.033	1.003±0.055	0.553±0.047	0.526±0.050
0.464	0.711±0.032	0.981±0.051	0.521±0.043	0.564±0.050	0.700±0.033	0.979±0.055	0.496±0.045	0.526±0.054
0.480	0.702±0.033	1.052±0.062	0.579±0.047	0.629±0.056	0.692±0.034	1.056±0.068	0.557±0.049	0.597±0.061
0.496	0.633±0.031	1.094±0.069	0.608±0.051	0.607±0.061	0.621±0.032	1.102±0.076	0.588±0.053	0.574±0.065
0.512	0.599±0.031	1.002±0.069	0.544±0.055	0.490±0.064	0.588±0.032	0.998±0.074	0.521±0.057	0.449±0.068
0.528	0.652±0.039	0.958±0.069	0.555±0.055	0.533±0.069	0.641±0.040	0.954±0.074	0.534±0.058	0.498±0.074
0.544	0.781±0.054	1.076±0.090	0.640±0.066	0.618±0.083	0.774±0.055	1.081±0.096	0.625±0.069	0.594±0.088
0.560	0.731±0.054	1.092±0.102	0.646±0.076	0.538±0.088	0.723±0.056	1.098±0.108	0.632±0.079	0.512±0.092
0.576	0.684±0.053	0.945±0.095	0.403±0.070	0.582±0.109	0.677±0.054	0.942±0.100	0.385±0.072	0.561±0.114
0.592	0.833±0.076	0.874±0.105	0.618±0.087	0.334±0.101	0.833±0.076	0.871±0.105	0.617±0.087	0.325±0.102

TABLE XIX: The deuteron over proton ($R_{D/H}$= D/H) and aluminum over deuteron ($R_{Al/D}$=Al/D) ratios for π^+ and π^- versus P_t^2 (in GeV$^2/c^2$). Left (right) part of the table represents the ratios before (after) events from diffractive ρ decay have been subtracted. Error bars are statistical only.

P_t^2	$R^+_{D/H}\pm$dR	$R^-_{D/H}\pm$dR	$R^+_{Al/D}\pm$dR	$R^-_{Al/D}\pm$dR	$R^+_{D/H}\pm$dR	$R^-_{D/H}\pm$dR	$R^+_{Al/D}\pm$dR	$R^-_{Al/D}\pm$dR
0.004	0.724±0.017	0.922±0.024	0.646±0.027	0.623±0.031	0.709±0.018	0.912±0.027	0.618±0.029	0.573±0.035
0.012	0.739±0.018	0.975±0.029	0.633±0.027	0.538±0.030	0.723±0.018	0.972±0.033	0.603±0.029	0.477±0.034
0.020	0.781±0.020	0.925±0.035	0.602±0.027	0.698±0.039	0.767±0.021	0.915±0.039	0.569±0.029	0.656±0.044
0.028	0.711±0.020	0.973±0.045	0.624±0.031	0.588±0.038	0.692±0.021	0.969±0.051	0.589±0.034	0.530±0.043
0.036	0.766±0.024	0.942±0.050	0.550±0.031	0.564±0.041	0.750±0.025	0.934±0.057	0.516±0.034	0.500±0.046
0.044	0.741±0.024	0.944±0.056	0.560±0.034	0.567±0.046	0.722±0.026	0.935±0.064	0.519±0.037	0.500±0.052
0.052	0.694±0.024	0.898±0.060	0.593±0.038	0.596±0.053	0.674±0.026	0.883±0.068	0.565±0.041	0.527±0.060
0.060	0.722±0.027	0.998±0.076	0.590±0.040	0.584±0.055	0.702±0.029	0.986±0.089	0.550±0.044	0.516±0.063
0.068	0.757±0.031	1.034±0.086	0.673±0.046	0.565±0.060	0.739±0.033	1.040±0.101	0.639±0.050	0.493±0.068
0.076	0.782±0.034	0.899±0.082	0.515±0.043	0.679±0.077	0.765±0.037	0.881±0.095	0.466±0.047	0.619±0.090
0.084	0.718±0.035	0.827±0.077	0.720±0.057	0.633±0.075	0.694±0.037	0.799±0.087	0.687±0.063	0.565±0.086
0.092	0.738±0.037	0.948±0.100	0.614±0.054	0.642±0.080	0.717±0.039	0.928±0.117	0.571±0.059	0.580±0.092
0.100	0.705±0.037	1.181±0.138	0.621±0.058	0.651±0.083	0.681±0.039	1.217±0.172	0.579±0.064	0.589±0.097
0.108	0.717±0.042	1.054±0.127	0.660±0.067	0.712±0.095	0.692±0.045	1.066±0.157	0.616±0.075	0.651±0.113
0.116	0.723±0.045	0.932±0.112	0.610±0.067	0.638±0.096	0.699±0.048	0.919±0.132	0.563±0.074	0.561±0.114
0.124	0.762±0.055	0.886±0.117	0.563±0.075	0.832±0.121	0.739±0.060	0.864±0.137	0.507±0.083	0.795±0.147
0.132	0.729±0.060	0.978±0.142	0.717±0.098	0.541±0.104	0.704±0.064	0.973±0.172	0.680±0.110	0.442±0.123
0.140	0.769±0.072	0.885±0.135	0.688±0.108	0.446±0.104	0.745±0.078	0.862±0.160	0.918±0.143	0.318±0.124
0.148	0.714±0.074	0.794±0.140	0.614±0.114	0.550±0.138	0.687±0.080	0.753±0.163	0.560±0.129	0.432±0.168
0.156	0.800±0.093	1.164±0.264	0.551±0.120	0.465±0.143	0.783±0.100	1.208±0.345	0.500±0.132	0.345±0.170
0.164	0.843±0.142	1.441±0.589	0.918±0.217	1.269±0.384	0.821±0.159	1.758±1.195	0.905±0.252	1.378±0.561
0.172	0.695±0.127	1.092±0.398	0.536±0.192	0.680±0.265	0.662±0.138	1.057±0.525	0.458±0.221	0.583±0.335
0.180	0.800±0.175	0.553±0.198	0.661±0.251	0.364±0.272	0.781±0.190	0.484±0.215	0.619±0.281	0.160±0.345
0.188	1.157±0.392	0.744±0.328	0.817±0.357	0.597±0.367	1.185±0.472	0.696±0.376	0.790±0.409	0.488±0.453
0.196	0.850±0.352	0.545±0.604	0.518±0.415	2.079±2.119	0.836±0.382	0.412±0.698	0.466±0.456	2.849±4.515

[6] F. E. Close, F. J. Gilman and I. Karliner, Phys. Rev. D **6**, 2533 (1972).
[7] F. E. Close and F. J. Gilman, Phys. Lett. **B38**, 541 (1972).
[8] F. E. Close, H. Osborn, A. M. Thomson, Nucl. Phys. **B77**, 281 (1974).
[9] X. Ji, J.-P. Ma, F. Yuan, Phys. Lett. **B597**, 299 (2004).
[10] C. E. Carlson, Physics & Instrumentation with 6-12 GeV Beams, Thomas Jefferson Laboratory Accelerator Facility, Ed. S. Dytman, H. Fenker, P. Roos, p. 17 (1998)
[11] A. Afanasev, C. E. Carlson, and C. Wahlquist, Phys. Rev. D **62**, 074011 (2000).
[12] F. E. Close and N. Isgur, Phys. Lett. **B509**, 81 (2001).
[13] T. Navasardyan *et al.*, Phys. Rev. Lett. **98**, 022001 (2007).
[14] F. E. Close and W. Melnitchouk, Phys. Rev. C **68**, 035210 (2003).
[15] J. T. Dakin, G. J. Feldman, F. Martin, M. L. Perl, and W. T. Toner, Phys. Rev. Lett. **31**, 786 (1973).
[16] M. Stratmann and W. Vogelsang, Nucl. Phys. **B496**, 41 (1997); D. de Florian and R. Sassot, Phys. Rev. D **56**, 426 (1997).
[17] A. S. Raskin and T. W. Donnelly, Ann. Phys. (N.Y.) **191**, 78 (1989).
[18] J. Binnewies, B. A. Kniehl, and G. Kramer, Phys. Rev. D **52**, 4947 (1995).
[19] E. L. Berger, Nucl. Phys. **B85**, 61 (1975).
[20] E. L. Berger, Proc. of the Workshop on Electronuclear Physics with Internal Targets, Stanford, CA, January 5-7, 1987.
[21] P. J. Mulders, in: R. G. Milner (Ed.), EPIC 2000: Proceeding of the 2nd Workshop on Physics with an Electron Polarized Light Ion Collider, Cambridge, MA, 2000; arXiv:hep-ph/0010199v1, 2000.
[22] W. Melnitchouk, R. Ent and C. E. Keppel, Phys. Rep. **406**, 127 (2005).
[23] W. Melnitchouk, AIP Conf. Proc. **588**, 267 (2001).
[24] J. L. Siegrist *et al.*, Phys. Rev. D **26**, 969 (1982).
[25] G. Hanson *et al.*, Phys. Rev. D **26**, 991 (1982).
[26] G. Drews *et al.*, Phys. Rev. Lett. **41**, 1433 (1978).
[27] F. E. Close and W. Melnitchouk, Phys. Rev. C **79**, 055202 (2009).
[28] N. Isgur, S. Jeschonnek, W. Melnitchouk and J. W. Van Orden, Phys. Rev. D **64**, 054005 (2001).
[29] I. Niculescu, Ph.D. thesis, Hampton University, 1999.
[30] I. Niculescu *et al.*, Phys. Rev. Lett. **85**, 1182 (2000).
[31] I. Niculescu *et al.*, Phys. Rev. Lett. **85**, 1186 (2000).
[32] M. Glück, E. Reya, and A. Vogt, Eur. Phys. J. C **5**, 461 (1998).
[33] C. E. Carlson, N. C. Mukhopadhyay, Phys. Rev. D **58**, 094029 (1998).
[34] C. E. Carlson, F. J. Gilman, Phys. Rev. D **7**, 2258 (1973).
[35] G. Baum *et al.*, Phys. Rev. Lett. **45**, 2000 (1980).
[36] K. Abe *et al.*, Phys. Rev. Lett. **78**, 815 (1997).
[37] K. Abe *et al.*, Phys. Rev. D **58**, 112003 (1998).
[38] A. Airapetian *et al.*, Phys. Rev. Lett. **90**, 092002 (2003).
[39] R. Fatemi *et al.*, Phys. Rev. Lett. **91**, 222002 (2003).
[40] P. Solvignon *et al.*, Phys. Rev. Lett. **101**, 182502 (2008)
[41] A. Airapetian *et al.*, Phys. Lett. **B442**, 484 (1998).
[42] B. Adeva *et al.*, Phys. Rev. D **58**, 112001 (1998).
[43] P. L. Anthony *et al.*, Phys. Lett. **B493**, 19 (2000).
[44] J. Yun *et al.*, Phys. Rev. C **67**, 055204 (2003).
[45] A. Calogeracos, N. Dombey, and G. B. West, Phys. Rev. D **51**, 6075 (1995).
[46] P. Eden, P. Hoyer, and A. Khodjamirian, JHEP **0110**, 040 (2001).
[47] T. Sloan, G. Smadja, and R. Voss, Phys. Rep. **162**, 45 (1988).
[48] K. Ackerstaff *et al.*, Phys. Rev. Lett. **81**, 5519 (1998).
[49] E. A. Hawker *et al.*, Phys. Rev. Lett. **80**, 3715 (1998); J. C. Peng *et al.*, arXiv:hep-ph/9804288v1, 1998.
[50] C. J. Bebek *et al.*, Phys. Rev. Lett. **34** (1975) 759.
[51] C. J. Bebek, A. Browman, C. N. Brown, K. M. Hansen, R. V. Kline, D. Larson, F. M. Pipkin, S. W. Raither, A. Silverman, and L. K. Sisterson, Phys. Rev. Lett. **37**, 1525 (1976).
[52] C. J. Bebek, C. N. Brown, M. S. Herzlinger, S. D. Holmes, C. A. Lichtenstein, F. M. Pipkin, S. W. Raither, and L. K. Sisterson, Phys. Rev. D **15**, 3085 (1977).
[53] J. Ashman *et al.*, Phys. Lett. **B206**, 364 (1988), Nucl. Phys. **B328**, 1 (1989). M. Arneodo *et al.*, Nucl. Phys. **B321**, 541 (1989).
[54] P. L. Anthony *et al.*, Phys. Lett. **B458**, 529 (1999); **B463**, 339 (1999); **B493**, 19 (2000).
[55] K. Ackerstaff *et al.*, Phys. Lett. **B404**, 383 (1997); **B444**, 521 (1998); A. Airapetian *et al.*, Phys. Lett. **B442**, 484 (1998).
[56] J. Adams *et al.*, Phys. Rev. Lett. **92**, 171801 (2004); S. S. Adler *et al.*, Phys. Rev. Lett. **91**, 241803 (2003).
[57] M. Anselmino, M. Boglione, U. D'Alesio, A. Kotzinian, F. Murgia and A. Prokudin, AIP Conf. Proc. **792**, 981 (2005); Phys. Rev. D **71**, 074006 (2005); M. Anselmino, M. Boglione, A. Prokudin and C. Turk, Eur. Phys. J. A **31**, 373 (2007).
[58] R. N. Cahn, Phys. Lett. **B78**, 269 (1978); Phys. Rev. D **40**, 3107 (1989).
[59] J. Levelt and P. J. Mulders, Phys. Rev. D **49**, 96 (1994).
[60] E. L. Berger, T. Gottschalk, and D. W. Sivers, Phys. Rev. D **23**, 99 (1981).
[61] K. Oganessyan, H. R. Avakian, N. Bianchi, P. Nezza, Eur. Phys. J. C **5**, 681 (1998).
[62] A. Metz, Phys. Lett. **B549**, 139 (2002).
[63] A. Bacchetta, M. Diehl, K. Goeke, A. Metz, P. Mulders and M. Schlegel, JHEP **0702**, 093 (2007).
[64] D. Boer and P. J. Mulders, Phys. Rev.D **57**, 5780 (1998); Nucl. Phys. **B564**, 471 (2000); D. Boer and R. D. Tangerman, Nucl. Phys. **B461**, 197 (1996).
[65] V. Barone, Z. Lu and B-Q. Ma, arXiv:hep-ph/0512145v1, 2005.
[66] L. P. Gamberg, G. R. Goldstein, and M. Schlegel, Phys. Rev. D **77**, 094016 (2008).
[67] R. Ent, H. Mkrtchyan and G. Niculescu, TJNAF Experiment E00-108, 2000.
[68] H. P. Blok *et al.*, Phys. Rev. C **78**, 045202 (2008).
[69] R. Asaturyan *et al.*, Nucl. Instrum. Methods Phys. Res. A **548**, 364 (2005).
[70] L. W. Mo and Y. S. Tsai, Rev. Mod. Phys. **41**, 205 (1969).
[71] R. Ent, B. W. Filippone, N. C. R. Makins, R. G. Milner, T. G. O'Neill and D. A. Wasson, Phys. Rev. C **64**, 054610 (2001).
[72] D. M. Koltenuk, Ph.D. thesis, University of Pennsylvania, 1999.
[73] D. Gaskell, Ph.D. thesis, Oregon State University, 2001.
[74] I. Akushevich, A. Ilyichev, N. Shumeiko, A. Soroko,

A. Tolkachev, Comp. Phys. Comm. **104**, 201 (1997).
[75] T. V. Kuchto and N. M. Shumeiko, Nucl. Phys. **B219**, 412 (1983).
[76] I. Akushevich and N. M. Shumeiko, J. Phys. G: Nucl. Part. Phys. **20**, 513 (1994).
[77] P. Brauel, T. Canzler *et al.*, Z. Physik C **3**, 101 (1979).
[78] V. Tadevosyan *et al.*, Phys. Rev. C **75**, 055205 (2007).
[79] T. Horn *et al.*, Phys. Rev. Lett. **97**, 192001 (2006).
[80] D. Drechsel, S. S. Kamalov, and L. Tiator, Nucl. Phys. **A645**, 145 (1999).
[81] I. Akushevich, N. Shumeiko, and A. Soroko, Euro. Phys. J. C **10**, 681 (1999).
[82] T. Sjostrand, L. Lonnblad, S. Mrenna, and P. Skands, arXiv:hep-ph/0308153v1, 2003.
[83] P. Liebing, Ph.D. dissertation, University of Hamburg, 2004.
[84] C. Hadjidakis, Ph.D. dissertation, Institut de Physique Nucleaire Orsay, 2002.
[85] H. Avagyan, private communication.
[86] T. Navasardyan, Ph.D. dissertation, Yerevan Physics Institute, 2007.
[87] H. Mkrtchyan, doctoral dissertation, Yerevan Physics Institute, 2008.
[88] M. M. Sargsyan, private communications (2005).
[89] Hall C Monte-Carlo package for SIDIS, JLab Hall C documents, http://www.jlab.org/Hall-C/.
[90] H. L. Lai, J. Huston, S. Kuhlmann, J. Morfin, F. Olness, J. F. Owens, J. Pumpin and W. K. Tung, Eur. Phys. J. C **12**, 375 (2000).
[91] P. Geiger, Ph.D. dissertation, Heidelberg University, 1998.
[92] B. Hommez, Ph.D. dissertation, University Gent, 2003.
[93] H. Mkrtchyan, El. J. Contemp. Phys. (Armenian Academy Sciences) **43**, 266 (2008); Izv. NAN Armenii, Fizika **43**, 410 (2008).
[94] H. Mkrtchyan *et al.*, Phys. Lett. **B665**, 20 (2008).
[95] H. Mkrtchyan, El. J. Nat. Sciences, NAS RA **1**, 12 (2009).
[96] A.G.S. Osborne, Ph.D. dissertation, Glasgow University, 2006.
[97] C. J. Bebek, C. N. Brown, R. V. Kline, F. M. Pipkin, S. W. Raither, L. K. Sisterson, A. Browman, K. M. Hanson, D. Larson and A. Silverman, Phys. Rev. D **16**, 1986 (1977).
[98] A. Airapetian *et al.*, Eur. Phys. J. C **21**, 599 (2001).
[99] G. Jones *et al.*, Z. Phys. C **62**, 601 (1994)
[100] A. Airapetian *et al.*, Nucl. Phys. **B780**, 1 (2007)
[101] A. Bialas and T. Chmaj, Phys. Lett. **B133**, 241 (1983).
[102] K. Galmeister and U. Mosel, Nucl. Phys. **A801**, 68 (2008).
[103] A. Accardi, V. Muccifora and H. J. Pirner, arXiv:nucl-th/0211011v4, 2003.
[104] J. Gomez *et al.*, Phys. Rev. D **49**, 4348 (1994).
[105] Y. Van Haarlem, for the HERMES collaboration, Proceedings of 9th Workshop on Non-Perturbative Quantum Chromodynamics, Paris, France, June 4-8, 2007.
[106] J. J. van Hunen, Ph.D. thesis, Utrecht University, 2000.
[107] I. C. Cloet, W. Bentz and A. W. Thomas, Phys. Rev. Lett. **102**, 252301 (2009).
[108] D. Dutta, D. Gaskell and K. Hafidi, JLab Proposal PR12-09-004, 2009.
[109] D. Dutta, J.-C. Peng, I. C. Cloet and D. Gaskell, Phys. Rev. C **83**, 042201 (2011).
[110] P. Schweitzer, T. Teckentrup and A. Metz, Phys. Rev. D **81**, 094019 (2010).
[111] M. Osipenko *et al.*, Phys. Rev. D **80**, 032004 (2009).
[112] M. Lacombe *et al.*, Phys. Rev. C **21**, 861 (1980).
[113] R. Jakob, P. J. Mulders, and J. Rodrigues, Nucl. Phys. **A626**, 937 (1997).
[114] Bino Maiheu, Ph.D. thesis, Universiteit Gent, 2006.
[115] Ph. Hagler, B. U. Musch, J. W. Negele, and A. Schafer, Europhys. Lett. **88**, 61001 (2009).